

Estimating Time-Varying Epidemic Severity Rates with Adaptive Deconvolution

Jeremy Goldwasser* Addison J. Hu† Alyssa Bilinski‡ Daniel J. McDonald§
 Ryan J. Tibshirani*

Abstract

Several key metrics in public health convey the probability that a primary event will lead to a more serious secondary event in the future. These “severity rates” can change over the course of an epidemic in response to shifting conditions like new therapeutics, variants, or public health interventions. In practice, time-varying parameters such as the case-fatality rate are typically estimated from aggregate count data. Prior work has demonstrated that commonly-used ratio-based estimators can be highly biased, motivating the development of new methods. In this paper, we develop an adaptive deconvolution approach based on approximating a Poisson-binomial model for secondary events, and we regularize the maximum likelihood solution in this model with a trend filtering penalty to produce smooth but locally adaptive estimates of severity rates over time. This enables us to compute severity rates both retrospectively and in real time. Experiments based on COVID-19 death and hospitalization data, both real and simulated, demonstrate that our deconvolution estimator is generally more accurate than the standard ratio-based methods, and displays reasonable robustness to model misspecification.

1 Introduction

Many important public health metrics report the probability that a secondary, often more severe outcome, follows a given primary event. The most common of these “severity rates” is the case-fatality rate, or CFR (Cao et al., 2020; Garske et al., 2009). This is sometimes treated as a proxy for the infection-fatality rate, or IFR, which is generally more challenging to compute (Luo et al., 2021; COVID-19 Forecasting Team, 2022). Other examples of interest are based on different types of primary events, for example hospitalizations (Bellan et al., 2020) and wastewater shedding (Xiao et al., 2022).

It is common to treat severity rates as stationary over time (Ghani et al., 2005; Jewell et al., 2007; Reich et al., 2012; Baud et al., 2020). This assumes that the population-level probability of developing a secondary event, given a primary event, is constant throughout the entire epidemic. In reality, however, severity rates often vary in time—due to evolving factors like the introduction of vaccines (di Lego et al., 2022), improved treatments (Hammond et al., 2022), and the emergence of new variants (Li et al., 2023a). For example, Xia et al. (2024) estimates the original COVID-19 variant to have a 3.6% CFR globally, compared to 2.0% for the Delta variant, and 0.7% for Omicron. .

In an ideal setting, severity rates could be calculated directly using detailed line-list or claims data that track outcomes of individual patients (Bellan et al., 2020; Challen et al., 2021; Roth et al., 2021; Xie et al., 2024). However, during fast-moving epidemics like COVID-19, comprehensive real-time tracking on a large geographic scale has generally been impractical. As a result, severity rates are commonly estimated using aggregate counts of primary and secondary events over time. Indeed, CFR estimates based on aggregate case and death counts became ubiquitous during the COVID-19 pandemic. These appeared not only in scientific studies (Liu et al., 2023; Wjst and Wendtner, 2023; Rajgor et al., 2020), but also in major news outlets such as The Atlantic (Madrigal and Moser, 2020), Wall Street Journal (Kamp and Krouse, 2020), and New York Times (McNeil, 2020).

*Department of Statistics, University of California, Berkeley

†Department of Statistics and Machine Learning Department, Carnegie Mellon University

‡Departments of Health Policy and Biostatistics, Brown University

§Department of Statistics, University of British Columbia

In this paper, we focus on estimating the severity rate, defined as

$$p_t = \mathbb{P}(\text{secondary event will occur} \mid \text{primary event at } t), \quad (1)$$

at each given point in time t . Severity rates can be estimated *retrospectively*, where data collected after time t is used to estimate p_t . Retrospective analyses can be valuable, as they can provide insights into epidemic dynamics amidst changing conditions. Often of greater interest, however, is estimating severity rates in *real time*, which means only data available up until t may be used to estimate p_t . This is far more challenging, and expanding (1) helps explain why: we have $p_t = \sum_{k=0}^{\infty} \mathbb{P}(\text{secondary event occurs at } t+k \mid \text{primary event at } t)$, which depends on epidemic events (of potentially changing likelihood) in the future, yet real-time estimators for p_t may only use data through t , and none afterwards.

Common methods for constructing real-time severity rate estimates are based on taking ratios of primary and secondary event counts. These are described later in Section 4.2. In past work (Goldwasser et al., 2024), we demonstrated that such ratio-based estimators can be subject to large (and predictable) statistical biases. Common retrospective estimators take on similar forms, and generally exhibit similar biases.

In this work, we propose an approach that overcomes the limitations of these methods. Our method has less bias than the existing ratio-based estimators, as it is based on performing deconvolution in a model that explicitly encodes time-varying severity rates in order to generate secondary events from primary events. At its core, our deconvolution model stems from a Poisson-binomial characterization of the relationship between primary and secondary event counts. Since this model is underspecified, we use regularization—specifically, a form of trend filtering—to smooth out the estimated severity rates, while maintaining the ability to adapt to potentially abrupt changes in the underlying signal (thanks to the local adaptivity of trend filtering). In the real-time case, we use additional regularization at the right tail of the sequence, originally developed in Jahja et al. (2022). Our work expands on Qu et al. (2022), which proposes to estimate severity rates using a similar but more restricted framework, based on squared loss and total variation penalties.

We validate our methodology on a broad range of experiments. These experiments start with real data on COVID-19 hospitalizations during the pandemic, and hypothetical hospitalization-fatality rate (HFR) curves that we craft based on associating the major four variants (original strain, Alpha, Delta, and Omicron) with fixed but data-driven HFRs. We then simulate COVID-19 deaths using a Poisson-binomial (or beta-binomial, in cases where overdispersion is present) model which uses observed hospitalization counts and hypothetical HFR curves. Tuning all hyperparameters with cross-validation, our deconvolution method averages over 15% lower MAE than the convolutional ratio estimator in the retrospective case. This improvement increases to 55% when comparing to the lagged ratio, arguably the standard choice in current practice (Yuan et al., 2020; Luo et al., 2021; Horita and Fukumoto, 2022; Feng et al., 2023; Liu et al., 2023). The benefits in the real-time case are similarly strong. Our method continues to outperform ratio-based methods under various degrees of model misspecification. Lastly, the same qualitative benefits are observed on real COVID-19 deaths.

The rest of this article is structured as follows. In Section 2, we develop the Poisson-binomial model and corresponding approximations used for deconvolution. In Section 3, we introduce our approaches for severity rate estimation, in both retrospective and real-time cases. In Section 4, we describe our simulation setup, and in Section 5, we analyze its results. In Section 6, we analyze and compare HFR estimates on real COVID-19 deaths. In Section 7, we conclude with a discussion.

2 Statistical model

In this section, we present a model which relates secondary to primary event counts, via severity rates, and describe an approximate likelihood suitable for inference.

2.1 Exact likelihood

At a time point t , let X_t and Y_t be the aggregate numbers of primary and secondary events, respectively. In the context of CFR, for example, X_t would be the number of new cases at time t , and Y_t the number of new deaths. Throughout we consider discrete integer-valued time points such as $t = 1, 2, 3, \dots$, but allow negative time values, for notational simplicity (for example, when indexing the set of time points that precede a given time t , as we do below).

In general, the number of secondary events at time Y_t can be expressed as a sum of indicator functions, where each indicator represents whether a given primary in the past event resulted in a secondary event at t . Using cases and deaths as primary and secondary events, for concreteness, observe that

$$Y_t = \sum_{k=0}^{\infty} \sum_{i=1}^{X_{t-k}} \mathbb{1}\{\text{case } i \text{ occurring at time } t-k \text{ dies at } t\}. \quad (2)$$

The secondary incidence time series can be understood probabilistically by noting that the indicator functions are Bernoulli random variables. Applying the definition of conditional probability,

$$\begin{aligned} \mathbb{E}[\mathbb{1}\{\text{case } i \text{ at } t-k \text{ dies at } t\}] \\ = \mathbb{P}(\text{dies at } t \mid \text{case at } t-k) \\ = \mathbb{P}(\text{dies at any time} \cap \text{dies at } t \mid \text{case at } t-k) \\ = \mathbb{P}(\text{dies at any time} \mid \text{case at } t-k) \cdot \mathbb{P}(\text{dies at } t \mid \text{case at } t-k, \text{ dies at any time}). \end{aligned}$$

The first term of the final line is the severity rate p_{t-k} , from (1). Meanwhile, we define the second term to be the k^{th} element of the *delay distribution* at time $t-k$. Formally, define

$$\pi_k^{(t)} = \mathbb{P}(\text{dies at } t+k \mid \text{case at } t, \text{ dies at all})$$

as the k^{th} element of the delay distribution at time t , where $\sum_{k=0}^{\infty} \pi_k^{(t)} = 1$. Observe that we may then write

$$\mathbb{1}\{\text{case } i \text{ occurring at time } t-k \text{ dies at } t\} \sim \text{Bernoulli}(p_{t-k} \pi_k^{(t-k)}). \quad (3)$$

It is reasonable to assume that these Bernoulli random variables are independent. Each represents a different patient, whose fates should not affect one another. An exception could be if severity rates are being calculated within a very small group of people who share the same scarce resources, for example, if one person's death frees up hospital resources for others, marginally improving their prognosis. In general, however, severity rates are typically assessed over a broad population, at the resolution of counties or states or even countries—not single hospitals. Henceforth, we make the assumption that individual patient outcomes are independent.

Under this assumption, note that $Y_t \mid X_{s \leq t}$ follows a *Poisson-binomial* distribution, where we abbreviate $X_{s \leq t} = \{X_s : s \leq t\}$. The Poisson-binomial generalizes the binomial distribution, in that it represents a sum of Bernoulli random variables that do not necessarily share the same success probability. Indeed, combining (2) and (3), we may write

$$Y_t \mid X_{s \leq t} \sim \text{PoissonBinomial}\left(\underbrace{\pi_0^{(t)} p_t, \dots, \pi_0^{(t)} p_t}_{X_t}, \underbrace{\pi_1^{(t-1)} p_{t-1}, \dots, \pi_1^{(t-1)} p_{t-1}}_{X_{t-1}}, \dots\right), \quad (4)$$

where the underbraces indicate the number of times each success probability is repeated. A useful fact to record will be the mean and variance of this distribution:

$$\mu_t = \mathbb{E}[Y_t \mid X_{s \leq t}] = \sum_{k=0}^{\infty} X_{t-k} \pi_k^{(t-k)} p_{t-k}, \quad \text{and} \quad \sigma_t^2 = \text{Var}(Y_t \mid X_{s \leq t}) = \sum_{k=0}^{\infty} X_{t-k} \pi_k^{(t-k)} p_{t-k} (1 - \pi_k^{(t-k)} p_{t-k}). \quad (5)$$

which follow by linearity of expectation and independence.

Approximations to the Poisson-binomial. The Poisson-binomial likelihood is generally intractable for large counts. As with the binomial distribution, for the probability mass function at $Y_t = y_t$, it is necessary to consider all $\sum_{k=0}^{\infty} X_{t-k}$ choose y_t combinations of patients that may yield this realized number of secondary events. For the Poisson-binomial, however, these combinations do not share the same probability of occurring, since the Bernoulli variates in (4) have different success probabilities. As a result, evaluating the probability mass function requires enumerating all products of y_t Bernoulli probabilities. This combinatorial explosion is computationally prohibitive unless the total number of primary events is very small, which is not the case in our application, where we are concerned with COVID-19 cases or hospitalizations for U.S. states, or across the whole nation.

Fortunately, different approximations exist for the Poisson-binomial distribution. A natural choice is the Poisson distribution with rate μ_t from (5). This has nonnegative, albeit unbounded, support. It has variance $\sum_{k=0}^{\infty} X_{t-k} \pi_k^{(t-k)} p_{t-k}$, which is larger than σ_t^2 in (5), but this difference matters little in practice, at least in our applications of interest. For example, using numbers from the national experiments we run in Section 4, the Poisson variance is only bigger by about 1.28%. More formally, Barbour and Hall (1984) showed that the Poisson approximation to the Poisson-binomial incurs small error when the Bernoulli random variables have low success rates. This is generally true for severity rates in epidemics, where the probabilities $\pi_k^{(t-k)} p_{t-k}$ are small. By the results of Barbour and Hall (1984), the total variation distance between the Poisson-binomial in (4) and its corresponding Poisson approximation (with rate μ_t) is upper bounded by

$$\sum_{k=0}^{\infty} (\pi_k^{(t-k)} p_{t-k})^2.$$

Again employing data from our U.S. simulation, the above bound is only roughly 1.69×10^{-5} .

Alternatively, Hong (2013) studies a normal approximation to the Poisson-binomial, with mean μ_t and variance σ_t^2 . Their empirical and theoretical results show the normal approximation more faithfully captures the upper tail of the cumulative density function than the Poisson. However, it struggles with the lower tail when the mean is low, since it includes negative support.

Weak dependence at successive time points. Conditional on past counts of primary events, we have shown that secondary event counts follow a Poisson-binomial distribution. Strictly speaking, these secondary event counts need not be conditionally independent at successive time points, since they are defined over a common group of individuals. For example, if case i from $t-k$ dies at time t , then this same case cannot die at time $t+1$. Fortunately, the next result demonstrates that the counts from successive time steps are weakly dependent, under a simplifying assumption of equal variance.

Proposition 1. *Assume $\text{Var}(Y_t | X_{s \leq t}) = \text{Var}(Y_{t+1} | X_{s \leq t+1})$. Under the Poisson-binomial model described in (2), (3), (4), it holds that*

$$\text{Cor}(Y_t, Y_{t+1} | X_{s \leq t+1}) \in \left[\frac{-\max_{k \geq 0} \pi_k^{(t-k)} p_{t-k}}{1 - \max_{k \geq 0} \pi_k^{(t-k)} p_{t-k}}, 0 \right].$$

Appendix A contains the proof of this result. Given reasonably long-tailed delay distributions with low severity rates, each $\pi_k^{(t-k)} p_{t-k}$ will be quite small. Plugging in numbers corresponding to the national data considered in Section 4, the lower bound on the correlations from Proposition 1 is roughly -0.018. Computing the actual correlations from our simulated data, the lowest observed value is -0.012. As these numbers are so low, it seems reasonable to approximate the distribution of $Y_t | X_{s \leq t}$ as being independent over different time points t , for the sake of estimation.

2.2 Approximate likelihood

The previous subsection established that the distribution of $Y_t | X_{s \leq t}$ may be approximated by appropriately instantiated Poisson or Gaussian distributions, which are nearly conditionally independent of each other as t varies. In this subsection, we characterize the approximate likelihood (the joint distribution over t), leaving regularization to the next section. Let p denote the vector of severity rates, which has coordinate p_t at time t . By approximating the law of $Y_t | X_{s \leq t}$ as Poisson with rate $\mu_t = \mu_t(p)$ as in (5), and assuming independence of these conditional distributions over t , we arrive at the following maximum likelihood problem:

$$\begin{aligned} & \underset{0 \preceq p \preceq 1}{\text{maximize}} \prod_t \frac{\mu_t(p)^{Y_t} e^{-\mu_t(p)}}{Y_t!} \\ & \iff \underset{0 \preceq p \preceq 1}{\text{minimize}} \sum_t \left[\left(\sum_{k=0}^{\infty} X_{t-k} \pi_k^{(t-k)} p_{t-k} \right) - Y_t \log \left(\sum_{k=0}^{\infty} X_{t-k} \pi_k^{(t-k)} p_{t-k} \right) \right], \end{aligned} \quad (6)$$

where the notation $0 \preceq z \preceq 1$ denotes elementwise constraints. This optimization problem falls in the class of *Poisson linear inverse* problems, well-studied in statistical physics and image processing (Richardson, 1972;

Lucy, 1974; Dupé et al., 2011; Rond et al., 2016). For a Poisson linear inverse problem to be computationally tractable, the linear operator being applied to the optimization variable must have nonnegative entries. That is indeed the case here, as each of the terms $X_{t-k}\pi_k^{(t-k)}$ are nonnegative.

In most applications, the oracle delay distribution is unknown. In lieu of $\pi^{(t)}$, a plug-in estimate $\hat{\pi}^{(t)}$ can be used instead, which typically has a finite support, placing all of its mass on $[0, d]$, where $d < \infty$. In other words, this assumes that no secondary events occur after d time steps (and turns all infinite sums in (6) from $k = 0$ to ∞ into finite sums from $k = 0$ to d). In any case, whether or not the support of the delay distribution is finite, there will always be more severity rates than secondary event times, and so the maximum likelihood problem (6) is underspecified. The estimators we propose in Section 3 will thus use regularization.

Estimating the delay distributions $\pi^{(t)}$ is an entire line of work in and of itself. Many approaches use line lists which contain the times of primary and secondary events, other approaches may be based on parametric approximations (with a discretized gamma distribution being a popular choice), whose parameters are based on small observational studies or even chosen based on epidemiological literature. For a thorough account of existing methods, we refer the reader to Charniga et al. (2024).

We note that the identity-link parameterization used in (6) contrasts with Poisson regression, which is a generalized linear model that may be more familiar to many statisticians. In this model, the log of the rate is a linear function of the features, and we would learn parameters β such that $\log \mu_t = \sum_{k=0}^{\infty} X_{t-k}\pi_k^{(t-k)}\beta_{t-k}$. However, having estimated β , there would be no unique way to recover the severity rates p from

$$\log \left(\sum_{k=0}^{\infty} X_{t-k}\pi_k^{(t-k)}p_{t-k} \right) = \sum_{k=0}^{\infty} X_{t-k}\pi_k^{(t-k)}\beta_{t-k}.$$

Finally, in addition to the Poisson model described above, we also studied and implemented a severity rate estimator using the normal approximation. While both estimators performed roughly similarly well in our experiments, the Poisson model was simpler (note that the severity rates p appear in the variance in (5), which complicates the Gaussian approximation), and had marginally higher accuracy. For that reason, we only provide a high-level account of the Gaussian methods in the main text, delegating further discussion to Appendix B.

3 Severity rate estimators

We now present our proposed severity rate estimators for both the retrospective and real-time settings. We focus on the Poisson likelihood, with Appendix B covering the Gaussian case. Some form of regularization is necessary to compute likelihood-based severity rates, due to the fact that the maximum likelihood problem (either Poisson or Gaussian) is underspecified. While many forms of regularization would suffice to make the problem well-specified, we use a form which aligns with the smoothness considerations underlying severity rates, discussed in detail below. We then present our retrospective and real-time estimators.

3.1 Trend filtering regularization

Trend filtering is a nonparametric estimation technique, which models the mean function of univariate data as a piecewise polynomial where the order (e.g., linear or cubic) is user-specified (Kim et al., 2009). While this is reminiscent of the smoothing spline, trend filtering can adjust more responsively to the local level of smoothness in the underlying signal (Tibshirani, 2014) by adaptively selecting the locations—also called knots—at which the fitted polynomial changes. Local adaptivity is important for estimating severity rates, as these may remain constant for long stretches of time when epidemic conditions do not change substantially, before changing rapidly in response to new conditions.

For an integer order $m \geq 0$, trend filtering in its original form (for nonparametric regression) models the mean $\theta \in \mathbb{R}^n$ over n data points as a m^{th} degree piecewise polynomial. It does so by minimizing a loss term while penalizing the differences of θ of order $m+1$. These differences can be computed by multiplying θ by a difference operator $D^{(m+1)}$. This can be viewed as the discrete analog of a derivative operator, and is defined recursively as

$$D^{(m+1)} = D^{(1)} D^{(m)} \in \mathbb{R}^{(n-m-1) \times n}$$

where $D^{(1)}$ is the first difference operator

$$D^{(1)} = \begin{bmatrix} -1 & 1 & 0 & \cdots & 0 & 0 \\ 0 & -1 & 1 & \cdots & 0 & 0 \\ \vdots & \ddots & \ddots & \ddots & & \vdots \\ 0 & 0 & 0 & \cdots & -1 & 1 \end{bmatrix} \in \mathbb{R}^{(n-m-1) \times (n-m)}.$$

Trend filtering applies a penalty based on the ℓ_1 norm, $\lambda \|D^{(m+1)}\theta\|_1$, for a tuning parameter $\lambda \geq 0$. Since the ℓ_1 norm induces sparsity, trend filtering solutions $\hat{\theta}$ have the property that many elements of the differenced vector $D^{(m+1)}\hat{\theta}$ will be exactly zero (Tibshirani and Taylor, 2011), and generally more so for greater λ . The nonzero elements correspond to the knots, which are adaptively chosen based on the data. Between the knots, the solution traces out a m^{th} degree polynomial; different segments of $\hat{\theta}$ may possess more or less smoothness, depending on how close the knots are to each other. We refer to Tibshirani (2014) for more details, and to Tibshirani (2022) for more discussion of the broader context and relation to splines.

The special case of $m = 0$ produces a piecewise constant fit and is known as the fused lasso (Tibshirani et al., 2005) or total variation denoising (Rudin et al., 1992), and has a longer history of study. Recently, Qu et al. (2022) proposed to use a fused lasso penalty to estimate severity rates in a regression framework with squared loss. The methods detailed below can be understood as a generalization of their work, encompassing higher-order trend filtering penalties, a Poisson loss which stems from approximating the Poisson-binomial likelihood underlying secondary event generation (Section 2), and added tail regularization to tame real-time estimation (Section 3.3, below). That said, the squared loss used in Qu et al. (2022) is close to the Gaussian approximation we describe in Appendix B.

3.2 Retrospective deconvolution

Estimator. Our retrospective method appends a trend filtering penalty to the Poisson likelihood approximation derived in Section 2.2. In particular, starting from (6), we use a plug-in estimate $\hat{\pi}^{(t)}$ for the delay distribution, with finite support $[0, d]$, and append a trend filtering penalty of order $m \geq 0$, which yields

$$\underset{0 \leq p \leq 1}{\text{minimize}} \sum_t \left[\left(\sum_{k=0}^d X_{t-k} \hat{\pi}_k^{(t-k)} p_{t-k} \right) - Y_t \log \left(\sum_{k=0}^d X_{t-k} \hat{\pi}_k^{(t-k)} p_{t-k} \right) \right] + \lambda \|D^{(m+1)}p\|_1. \quad (7)$$

The above is a convex problem, and can be readily optimized with standard software. (Alternatively, we can adapt specialized approaches developed for trend filtering, as in Ramdas and Tibshirani (2016); Jahja et al. (2022), but we do not pursue this in the current paper). We denote the vector of retrospective severity rate estimates, obtained by solving (7), by \hat{p}^{rs} .

The sum in (7) is over all secondary event times. Let N_Y denote the number of such event times. Note that there are $N_Y + d$ estimated severity rates, starting at d time steps before the first secondary event time. Not all of these estimates are equally reliable. In this model, the severity rate p_t contributes to secondary events in the d time steps which follow. Away from the left or right boundary of second event times, assuming N_Y is sufficiently large relative to d , these secondary events are all observed. As a result, the estimate \hat{p}_t^{rs} is likely to be more stable, as it is contributes to (and is hence informed by) many elements of the loss.

On the other hand, severity rate estimates will be less stable when t is near the left or right boundaries of observations. In the most extreme edge cases, the first and last severity rates only affect a single secondary count. This data scarcity issue persists throughout the d time steps of each tail. As they contribute little to the loss, severity rate estimates at the tails are in general subject to greater variability. To account for this, we recommend (and implement) a burn-in and burn-out period for retrospective estimation. That is, while $N_Y + d$ severity rates are obtained, it is prudent to ignore the values near the boundaries.

Cross-validation. The hyperparameter $\lambda \geq 0$ in (7) controls the degree of smoothness exhibited by \hat{p}^{rs} . In an extreme case ($\lambda \rightarrow \infty$), the solution will take the form of a global polynomial of degree m . At the other extreme ($\lambda \rightarrow 0$), it will be a highly volatile piecewise polynomial, having a knot at each possible time point. We rely on K -fold cross-validation for selecting λ , defining folds in a structured way that respects the time dependence in our retrospective estimation problem. In each of the K folds, secondary incidence Y_t at

every K^{th} time step t is held out from the loss, reducing the number of training samples by a factor of $1/K$. For fold $j \in \{1, \dots, K\}$, denoting by $\hat{p}^{\text{rs},j}(\lambda)$ the result of optimizing the corresponding version of (7) with samples withheld, we record the mean absolute error (MAE) from deconvolution over the validation set V_j ,

$$\text{MAE}_j(\lambda) = \frac{1}{|V_j|} \sum_{t \in V_j} \left| Y_t - \sum_{k=0}^d X_{t-k} \hat{\pi}_k^{(t-k)} \hat{p}_{t-k}^{\text{rs},j}(\lambda) \right|.$$

The cross-validation error for the given λ is the average across the K folds:

$$\text{MAE}(\lambda) = \frac{1}{K} \sum_{j=1}^K \text{MAE}_j(\lambda).$$

This process is iterated over a grid of λ values, the largest of which should ideally produce an estimate with no knots. We denote this value by λ_{\max} , and derive its form in Appendix C. Observe that any $\lambda \geq \lambda_{\max}$ will result in an estimate which is a global polynomial. From the cross-validation error curve, we select the value λ^* of the tuning parameter with the lowest error, and then use this value to estimate severity rates using the whole time series. This is a standard strategy, sometimes called the “min rule.” An alternative that is useful when the cross-validation error curve is flat around its minimum is the “lse rule” (Hastie et al., 2009), which selects the largest λ whose cross-validation error is within one standard error of the minimum value.

Since fewer training samples are used when tuning λ in cross-validation, we make a slight adjustment to (7) in order to ensure that it balances the loss and regularization terms on a common scale. Specifically, whenever solving (7) (either in cross-validation iterations or in full, on the whole time series), we normalize each sum by its number of summands.

The order of trend filtering, $m \geq 0$, may also be tuned using the data. We can compare cross-validation errors across all λ and m , and select the pair (λ^*, m^*) with the lowest error. As we typically restrict our attention to $m \in \{0, 1, 2\}$ —resulting in piecewise constant, linear, and quadratic trends, respectively—such additional tuning over m does not present much of an additional computational burden. Alternatively, the user may want to handpick $m \in \{0, 1, 2\}$ based on qualitative considerations, to reflect the desired shape of the severity rate curve: piecewise constant, allowing for jump discontinuities; piecewise linear, allowing for sharp turnaround points; or piecewise quadratic, allowing for smoother evolution.

3.3 Real-time deconvolution

Estimator. Denote by T the time through which data is available and at which one seeks to estimate the current severity rate p_T . To be clear, in this real-time estimation problem, no data which becomes available after T may be used, since it does not yet exist. The most basic adaption of the retrospective approach in the previous subsection to the current real-time case would be to solve (7), where the sum is restricted to $t \leq T$. However, here the severity rate p_T only contributes only to a single data point Y_T in the loss function. This leads to a much greater degree of variability in estimating p_T compared to the retrospective case. We will therefore use extra regularization to temper such tail variability. This itself introduces a potential tradeoff, gaining stability but reducing adaptivity.

The regularization techniques we employ are inspired by Jahja et al. (2022), who studied deconvolution in the context of nowcasting infections that will eventually appear as case reports. The additional regularization comes in two parts. The first part is to impose a constraint on the tail values of the severity rate curve, which prevents overfitting to the most recent secondary counts. In particular, we constrain the differences of order $m+1$ of the last m severity rates to be zero, enforcing these rates to adhere to a polynomial trend of degree m (preventing a knot from occurring near the tail). This constraint differs only lightly from that in Jahja et al. (2022), who used a natural spline constraint. This constrains the tails to be a polynomial of degree $(m-1)/2$; note that our proposal applies to all values of m , whereas natural splines are only defined for odd m .

The second part adds a regularization term to the criterion which is a kind of tapered smoothing penalty, penalizing the squared differences $p_{t-1} - p_t$ in adjacent severity rates with successively decreasing weight as t moves away from T . Such weights are chosen based on how much mass is captured by the delay distribution between primary and secondary events. Specifically, we assign $(p_{t-1} - p_t)^2$ a weight $w_t = 1/\hat{F}^{(T)}(T-t)$ for

$t \geq T - d$, and $w_t = 0$ for $t < T - d$, where $\widehat{F}^{(T)}(k) = \sum_{j=0}^k \widehat{\pi}_j^{(T)}$ is the CDF of $\widehat{\pi}^{(T)}$ at k . Thus, the longer the tail of the delay distribution, the more we seek to smooth out severity rates in the recent past.

Putting these two sources of regularization together leads to the following optimization, which defines our real-time severity rate estimates at T :

$$\begin{aligned} & \underset{0 \leq p \leq 1}{\text{minimize}} \quad \sum_{t \leq T} \left[\left(\sum_{k=0}^d X_{t-k} \widehat{\pi}_k^{(t-k)} p_{t-k} \right) - Y_t \log \left(\sum_{k=0}^d X_{t-k} \widehat{\pi}_k^{(t-k)} p_{t-k} \right) \right] + \lambda \|D^{(m+1)} p\|_1 + \gamma \|WD^{(1)}\|_2^2 \\ & \text{subject to} \quad \sum_{k=0}^{m+1} (-1)^k \binom{m+1}{k} p_{T-m-1+k} = 0, \end{aligned} \quad (8)$$

where $W = \text{diag}(0, \dots, 0, \sqrt{w_{T-d}}, \dots, \sqrt{w_T})$ is a diagonal matrix whose only nonzero elements are the final $d+1$ diagonal entries. Denoting by \widehat{p}^{rt} the vector of real-time severity rate estimates obtained by solving (8), the real-time estimate of p_T is its last element $\widehat{p}_T^{\text{rt}}$.

In practice, it is common for epidemic data streams to be revised after initial data is released (Reinhart et al., 2021). This means that, from one time T to the next, the whole sequences of primary and secondary counts used in real-time estimation may be updated (rather than new primary and secondary counts simply being appended). To reflect this, it helps to introduce some additional notation: for time points $s \geq t$, denote by $X_t^{(s)}$ the version of primary incidence at time t which was available as of time s , and similarly $Y_t^{(s)}$ for secondary incidence. Therefore, in practice, we would substitute each pair X_t, Y_t of primary and secondary counts in (8) with $X_t^{(T)}, Y_t^{(T)}$, the versions of these counts available at T .

Cross-validation. We tune the hyperparameters $\lambda, \gamma \geq 0$ in (8) with a two-stage approach, again inspired by Jahja et al. (2022). First, setting $\gamma = 0$, tune λ with K -fold validation, exactly as in the retrospective case described previously. Then, fixing $\lambda = \lambda^*$ at the chosen value from cross-validation, we tune γ with a rolling-validation (also called forward-validation) procedure. This works as follows: for each $s = T - M, \dots, T - 1$, we solve (8) using only data up through time s , and use the resulting severity rate estimates $\widehat{p}^{\text{rt},s}(\gamma)$ to form a prediction $\widehat{Y}_{s+1}(\gamma)$ of Y_{s+1} by reconvolution. The rolling-validation error for the given γ is then

$$\text{MAE}(\gamma) = \frac{1}{M} \sum_{s=T-M}^{T-1} |\widehat{Y}_{s+1}(\gamma) - Y_{s+1}|.$$

This process is iterated over a grid of γ values. As with cross-validation, we can select a value γ^* according to the “min rule” (the γ with minimum MAE), or alternatively, the “1se rule” (the largest γ whose MAE lies within one standard error of the minimum). Finally, the real-time problem is solved at hyperparameter values λ^* and γ^* on all available data, from which we extract $\widehat{p}_T^{\text{rt}}$. This is summarized in Algorithm 1.

It is worth making two further remarks. First, as in the retrospective case, before running either cross-validation or forward-validation, the likelihood and regularizer terms in (8) are placed on a common scale by dividing each by their number of summands. Second, the order of trend filtering m can again be tuned using the two-stage approach, based on minimizing the forward-validation error. It can instead be chosen based on qualitative considerations, as discussed in the retrospective subsection.

4 Simulation setup

4.1 Ground truth construction and synthetic data generation

To evaluate our methods against existing benchmarks, we generated realistic secondary incidence data using ground truth severity rates, whose computation is described below. These simulations are intended to mimic true COVID-19 deaths in the U.S. over the pandemic. The severity rate we targeted throughout our analysis was hence the hospitalization-fatality rate (HFR).

Real data resources. Our simulations used real hospitalization counts as the primary incidence data. In the first several years of the pandemic, COVID-19 hospital admissions were reported daily in real time to the

Algorithm 1 Tuning λ, γ by two-stage validation

Input: Candidate sets of values Λ, Γ for λ, γ ; primary and secondary incidence X_t, Y_t , for $t \leq T$; number of cross-validation folds K and number of forward-validation steps M

Output: Selected λ^*, γ^*

- 1: **for** each $\lambda \in \Lambda$ **do**
- 2: Use K -fold cross-validation for problem (8) with $\gamma = 0$, to record $\text{MAE}(\lambda)$
- 3: **end for**
- 4: Select λ^* by min or 1se rule
- 5: **for** each $\gamma \in \Gamma$ **do**
- 6: **for** $s = T - M$ to $T - 1$ **do**
- 7: Solve (8) with given γ , $\lambda = \lambda^*$, and $T = s$ to yield $\hat{p}^{\text{rt},s}(\gamma)$
- 8: Linearly extrapolate $\hat{p}_{s+1}^{\text{rt},s}(\gamma)$ from $\hat{p}_s^{\text{rt},s}(\gamma)$ and $\hat{p}_{s-1}^{\text{rt},s}(\gamma)$
- 9: Compute prediction $\hat{Y}_{s+1}(\gamma) = \sum_{k=0}^d X_{s+1-k} \hat{\pi}_k^{(s)} \hat{p}_{s+1-k}^{\text{rt},s}(\gamma)$
- 10: **end for**
- 11: Record $\text{MAE}(\gamma) = \frac{1}{M} \sum_{s=T-M}^{T-1} |\hat{Y}_{s+1}(\gamma) - Y_{s+1}|$
- 12: **end for**
- 13: Select γ^* by min or 1se rule
- 14: **return** λ^*, γ^*

Department of Health and Human Services ([Department of Health and Human Services, 2023](#)). This process was coordinated by the National Healthcare Safety Network, thus we refer to the aggregate daily hospital admissions as NHSN data. We used the Epidata API to download this data ([Farrow et al., 2015](#)).

From observed NHSN hospitalizations, we simulated COVID-19 deaths across the U.S. and all 50 states, as well as for both the retrospective and real-time settings. We designed separate simulation models for each of these settings; the discrepancy here reflects the fact that different counts were available in real-time versus in retrospect during the pandemic. True weekly death totals were aggregated in retrospect by the National Center for Health Statistics ([Ahmad and Cisewski, 2025](#)). NCHS revealed these death totals well after the week in question. NHSN began comprehensive hospitalization reporting in summer 2020, and NCHS stopped reporting deaths in early 2023. Our retrospective simulations thus cover this 2.5-year window.

In real-time, Johns Hopkins University (JHU) published provisional daily death counts. These data bear a subtle yet important distinction from those of NCHS—JHU deaths reflect not the true number of deaths which occurred each day, but rather the number of new deaths *reported* on a given day. Often, these deaths were reported days or even weeks after they occurred. As a result, the delay distribution which underlies the JHU data has higher mean than that for NCHS. The JHU counts were also considerably noisier, due at least in part to reporting idiosyncrasies. Our real-time simulations cover the same 2.5-year window, from summer 2020 to early 2023, consistent with the retrospective case.

True severity rates. The severity rates that we used as the ground truth in our simulations were created using the following variant-based procedure. In each region (state or U.S. national), we defined a single HFR associated with the four most significant COVID-19 variants: the original strain, Alpha, Delta, and Omicron. Using data from CoVariants ([Hodcroft, 2021](#)), we identified the dominant period for each variant, based on when it accounted for over half of cases. Within this window, we computed the HFR as the total number of NCHS deaths divided by NHSN hospitalizations, offset by two weeks to account for delays. Finally, we mixed these per-variant HFRs with the variant proportions in circulation to obtain the final HFR curve:

$$p_t = \sum_v c_t^v p^v, \text{ where } \sum_v c_t^v = 1 \text{ for all } t.$$

Here the sums are over variants v , with p^v denoting the HFR for variant v , and c_t^v denotes the proportion of variant v in circulation at time t (calculated again from CoVariants data).

Delay distributions. While our severity rate estimators allow for nonstationary delay distributions $\pi^{(t)}$, our simulations use a constant delay $\pi^{(t)} = \pi$, for all t , for the sake of simplicity. Setting $d = 60$ days, we

fit discrete gamma distributions in each region parameterized by heuristically-chosen means and variances. The means were estimated by maximizing the cross-correlation between NHSN hospitalizations and deaths, NCHS deaths in the retrospective case and JHU in real-time. The standard deviations were set to 90% of the means, motivated by empirical findings on typical hospitalization-to-death delays (Ward and Johnsen, 2021). Denoting by F_γ the cumulative distribution function (CDF) of the corresponding gamma distribution, we define the delay distribution by $\pi_k \propto F_\Gamma(k+1) - F_\Gamma(k)$, where these values are normalized to sum to 1.

Noise models. Using the NHSN hospitalizations, variant-based severity rates, and delay distributions as described above, we then simulate daily deaths from the following noise models.

- For the retrospective simulation, we generated deaths from a Poisson-binomial model; this qualitatively matches the variance of death counts from NCHS, as shown in Figure 1.
- For the real-time simulation, we generated deaths from a beta-binomial distribution, which reflects the fact that JHU deaths are more overdispersed than what the Poisson-binomial can accommodate. As we describe below, we first estimated the amount of overdispersion, then simulated deaths with the given variance. The results qualitatively match the dispersion of deaths counts from JHU, see Figure 2.

To estimate the amount of dispersion in each region (50 states and U.S. overall), we first fit a smoothing spline to JHU deaths, after having cleaned the time series as described in Appendix D.1. This approximates the mean death curve, which under the Poisson-binomial model should roughly equal the variance of deaths across time. To estimate such variances, we compute squared residuals from the spline curve, and to assess the empirical relationship between means and variances, we run a univariate regression of these residuals on the spline fitted values, without intercept. The resulting coefficient $\hat{\beta}$ encodes the amount of overdispersion present in the JHU death data, in the given region. To accommodate such overdispersion in our simulation model for deaths, we then use a beta-binomial model, described next.

The beta-binomial distribution is a popular tool for modeling count data with dispersion (Kim and Lee, 2017). For our problem, in a given region with dispersion coefficient $\hat{\beta}$, we can use the standard mean-rho parameterization to define the beta-binomial at each time t , setting

$$M_t = \frac{\mu_t}{\sum_{k=0}^d X_{t-k}}, \text{ and } \rho_t = \left[\frac{\hat{\beta} \sigma_t^2}{\mu_t (1 - \mu_t / \sum_{k=0}^d X_{t-k})} - 1 \right] \left[\frac{1}{\sum_{k=0}^d X_{t-k} - 1} \right], \quad (9)$$

where μ_t and σ_t^2 are defined in (5). Appendix D.2 gives the details behind this calculation.

Figures 1 and 2 qualitatively assess the goodness-of-fit of our simulation models by plotting simulated and real data for four regions of varying sizes. While the curves do not overlap precisely (we do not have access to the true HFR in simulations), visual inspection shows that the noise levels are relatively comparable.

4.2 Methods considered

In the retrospective and real-time simulations, we ran Poisson deconvolution with trend filtering penalties of orders $m = 0, 1, 2$, which deliver piecewise constant, linear, and quadratic estimates, respectively. We further considered tuning the order m of trend filtering regularization itself, by cross-validation in the retrospective case, and forward-validation in real-time.

We compared these deconvolution methods to the standard ratio-based estimators of severity rates, which we will often refer to as to ‘‘benchmark’’ methods. The precise formulations for these methods differ slightly between the retrospective and real-time settings; in all cases, we allow the methods to use smoothed primary and secondary counts over some window $W \geq 1$, serving as a hyperparameter (with $W = 1$ corresponding to no smoothing). In the real-time setting, we smooth counts with a trailing window, and in retrospect, we use a centered window. For the case of primary incidence, define

$$\tilde{X}_t^{\text{rt}} = \frac{1}{W} \sum_{k=0}^{W-1} X_{t-k}, \text{ and } \tilde{X}_t^{\text{rs}} = \frac{1}{W} \sum_{k=-\lfloor W/2 \rfloor}^{\lceil W/2 \rceil - 1} X_{t+k},$$

and analogously define \tilde{Y}_t^{rt} and \tilde{Y}_t^{rs} for secondary incidence.

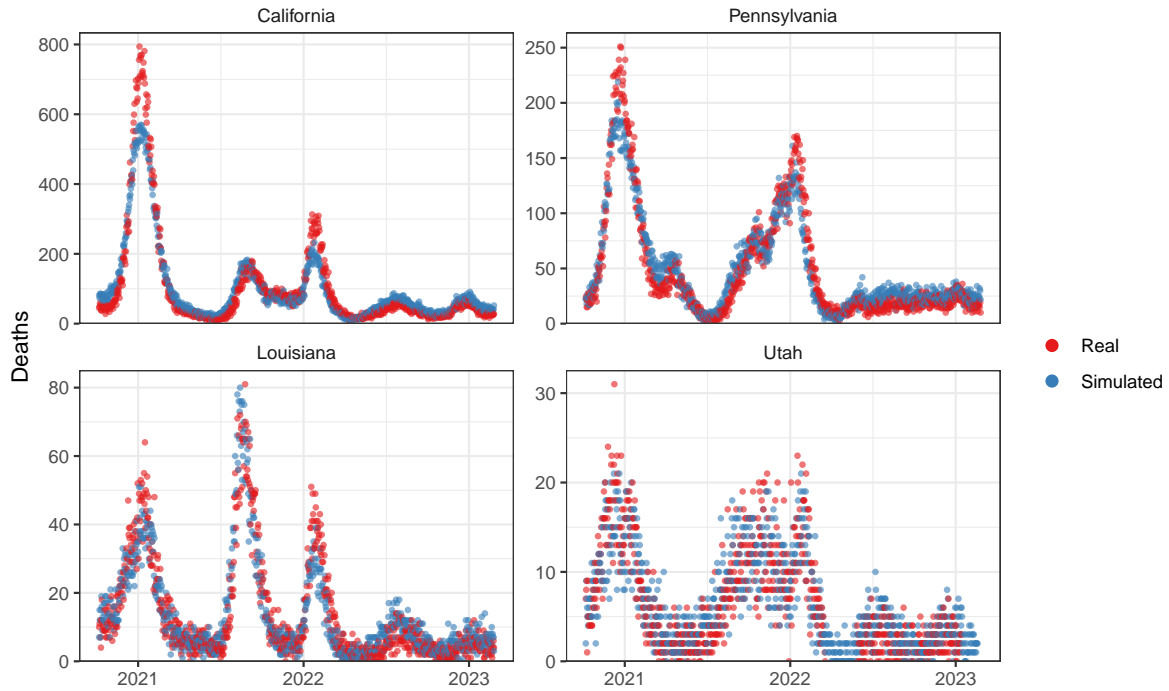


Figure 1: Real (NCHS) and simulated (Poisson-binomial) daily deaths. (The NCHS data is itself weekly, but here we have subsampled it to the daily level to match the time resolution of our simulated data.)

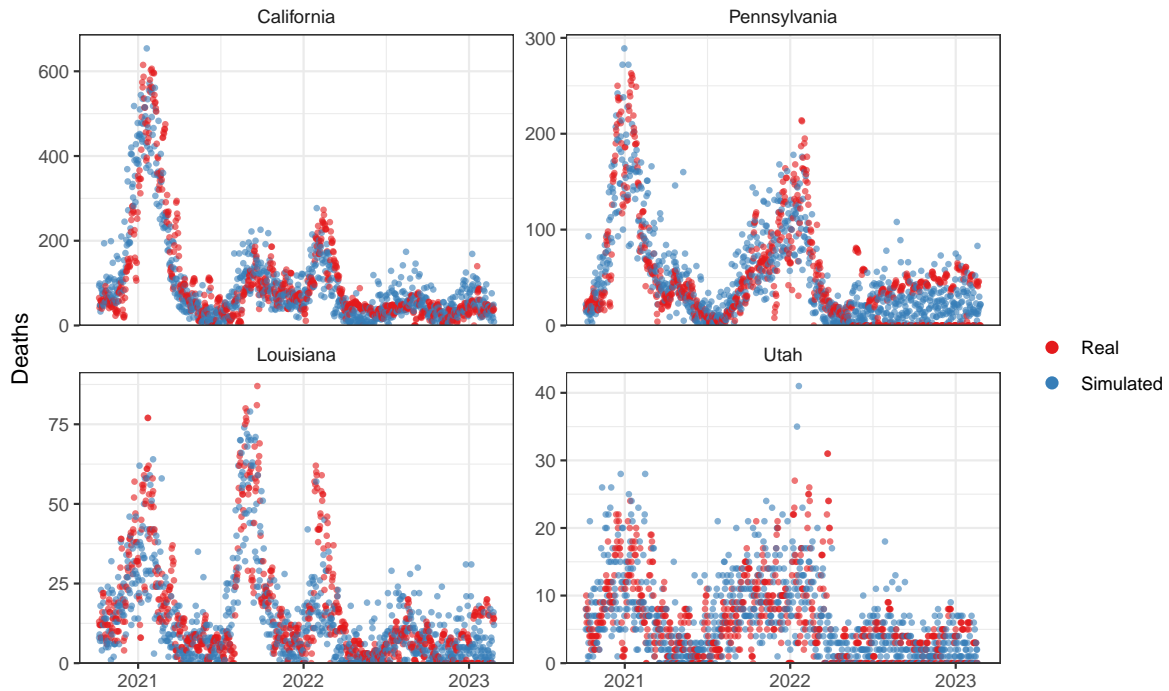


Figure 2: Real (JHU) and simulated (beta-binomial) daily deaths. (The JHU deaths displayed here are “finalized”, meaning that the history has been revised after the end of the reporting period. They have been preprocessed as described in Appendix D.1.)

With this notation in place we can now define the *lagged ratio* estimators, arguably the most widely-used estimators of severity rates in practice. These simply compare primary and secondary events, offset by a lag of $\ell \geq 0$ time steps. The real-time and retrospective lagged ratios are

$$\widehat{p}_t^{\text{rt}} = \frac{\tilde{Y}_t^{\text{rt}}}{\tilde{X}_{t-\ell}^{\text{rt}}}, \quad \text{and} \quad \widehat{p}_t^{\text{rs}} = \frac{\tilde{Y}_t^{\text{rs}}}{\tilde{X}_t^{\text{rs}}},$$

respectively. The lag parameter ℓ represents the typical duration between primary and secondary events.

Two alternative estimators introduced by [Overton et al. \(2022\)](#) (based on earlier work of [Nishiura et al. \(2009\)](#)) adopt a more faithful approach that uses an estimate of the delay distribution, $\widehat{\pi}^{(t)}$. We call these the *convolutional ratio* estimators, as the delay distribution convolves against trailing primary events to account for secondary incidence. The real-time convolutional ratio is

$$\widehat{p}_t^{\text{rt}} = \frac{\tilde{Y}_t^{\text{rt}}}{\sum_{k=0}^d \tilde{X}_{t-\ell}^{\text{rt}} \widehat{\pi}_k^{(t-k)}}.$$

The retrospective version tracks the proportion of cases among primary events at t who will eventually have secondary events. While secondary event dates for individual cases at t are unknown, the relevant secondary count can be estimated with a convolutional model. This leads to the retrospective convolutional ratio:

$$\widehat{p}_t^{\text{rs}} = \sum_{k=0}^d \frac{\tilde{Y}_{t+k}^{\text{rs}} \widehat{\pi}_k^{(t)}}{\sum_{j=0}^d \tilde{X}_{t+k-j}^{\text{rs}} \widehat{\pi}_j^{(t+k-j)}}.$$

We note that when each distribution $\widehat{\pi}^{(t)}$ is a point mass at ℓ , the convolutional ratios reduce to the lagged ones. Therefore, the former may be understood as generalizations of the latter.

In previous work [Goldwasser et al. \(2024\)](#), we studied the bias of the real-time lagged and convolutional ratios, both formally and empirically. Our analysis revealed that the lagged ratio tends to exhibit large bias, and can both signal nonexistent surges and fail to detect upticks in severity rate. The convolutional ratio is generally more robust, but it still can have significant bias when the severity rate is changing.

The retrospective lagged ratio is subject to roughly the same bias as in the real-time case: it is effectively the same estimator offset by ℓ time steps. The retrospective convolutional ratio is somewhat more challenging to analyze than its real-time counterpart. However, its derivation is based on a stationarity assumption, and it will still be particularly biased when the severity rate changes around t .

These ratio estimators all depend on the hyperparameter W , which controls the length of the smoothing window, and must be tuned. In the retrospective case, this is tuned via K -fold cross-validation, just like λ for the retrospective deconvolution method. In the real-time case, it is tuned via M -step forward-validation, just like γ for the real-time deconvolution method.

4.3 Experimental design

In all cases, we examined the use of both the min rule and the 1se rule to tune hyperparameters using cross- and forward-validation: recall this is λ for retrospective deconvolution; λ, γ for real-time deconvolution; and W for the benchmark methods, lagged and convolutional ratios, in both retrospective and real-time settings. In each case, we report results for the most favorable rule (min or 1se) in terms of MAE, giving each method the full benefit of the doubt; details will be given in the next section. We used $K = 5$ cross-validation folds and $M = 28$ forward-validation steps, throughout.

We evaluated deconvolution and benchmark severity rate estimators on simulated data across 50 states as well as the U.S. nationally. The estimation window encompassed a roughly two-year period between 2021 and 2022, omitting a burn-in and burn-out period. With the exception of the misspecified experiments described in the final paragraph of this subsection, the deconvolution methods and the convolutional ratios were given access to the oracle delay distribution, thus using $\widehat{\pi}^{(t)} = \pi$, for all t . The lagged ratios use a lag ℓ equal to the mean of the delay distribution in each region. In all but the misspecified experiments, the reported results are averaged over 10 replications (10 draws of data from the simulation model).

To perform deconvolution with trend filtering regularization we solved the optimization problems (7), (8) with Clarabel in CVXR ([Goulart and Chen, 2024](#)). The retrospective setting required much less computation

than real-time. For this reason, we also ran deconvolution and the benchmarks with oracle hyperparameter tuning. This selected the hyperparameters whose estimated severity rates had the smallest mean absolute error (MAE), in hindsight. To lessen the computational burden in both the retrospective and real-time cases, we only computed estimates from each method once every seven days. In total, this amounted to about 100 estimation dates, over which we calculated the eventual MAEs to be reported.

Lastly, we recomputed all the estimators under misspecified delay distributions—still constant over time, but not equal to π . We considered six different misspecified delay distributions with varying means; each was still a discrete gamma distribution, whose standard deviation is set to 90% of its mean. In the retrospective case, we set the means to be 1, 2, and 3 days before and after the true value for each state. For the real-time case, which had longer delay distributions, the means were offset by 1, 3, and 5 days, on both sides of the true value. Appendix D.3 provides visualizations of the misspecified delay distributions for a few states.

5 Simulation results

We analyze results across the synthetic experiments described in the previous section.

5.1 Retrospective analysis

In the retrospective setting, deconvolution largely outperforms the ratio-based estimators across the U.S. and the 50 states. Table 1 summarizes the performance of these methods when all of the hyperparameters are tuned via cross-validation. As mentioned above in the experimental design, we consider using both the min rule and 1se rule within cross-validation, and for each method we report the results from the rule with the strongest performance; in the retrospective case, this ends up being the 1se rule for each method. The table reports, for each method, the MAE averaged over the 51 regions and 10 replicates:

$$\frac{1}{51} \sum_{r=1}^{51} \left(\frac{1}{10} \sum_{i=1}^{10} \text{MAE}_{ri} \right),$$

where MAE_{ri} is the MAE for region r and replicate i . It also reports the associated standard error:

$$\sqrt{\frac{1}{51^2} \sum_{r=1}^{51} \frac{1}{10} \hat{\sigma}^2(\{\text{MAE}_{ri}\}_{i=1}^{10})},$$

where $\hat{\sigma}^2(S)$ is the sample variance of elements in a set S . In the table, “Deconv- m ” denotes deconvolution with trend filtering regularization of order m , and “Deconv-T” denotes deconvolution with the order tuned by cross-validation. The same labeling is used throughout all tables and figures.

As we can see from Table 1, all orders of trend filtering yield more accurate severity rate estimates than the ratio-based methods. The MAE of the convolutional ratio is roughly 8.3×10^{-3} on average, substantially outperforming the lagged ratio. For deconvolution methods, the average MAE ranges from 6.5 to 6.9×10^{-3} , depending on the order m . This translates to a roughly 14-18% improvement in MAE over the convolutional ratio, and roughly 54-56% over the lagged ratio. Tuning the order of trend filtering also works well. Moreover, Table 3 in Appendix E shows that under oracle tuning (with all tuning parameters chosen to optimize MAE) deconvolution outperforms the benchmarks by an even wider margin.

Figure 3A disaggregates the MAEs by population size, across the 51 regions. Observe that the spread of improvement varies by population, with deconvolution generally having stronger gains over the benchmarks for smaller population sizes (where estimation is generally more challenging). Figure 3B confirms that this holds for all orders of trend filtering regularization.

Figure 4 shows the HFR curves for an example region, Pennsylvania. The ratio-based estimates oscillate sharply around the ground truth (black line), with the lagged ratio displaying clearly greater volatility, but the convolutional ratio still showing a nontrivial amount as well. Broadly, the estimates from deconvolution do not share this behavior and are qualitatively more stable. We emphasize that this is the case even though all methods have used using cross-validation with the 1se rule to tune hyperparameters (which incentivizes a greater amount of regularization). This behavior is generally consistent across all geographies, and the HFR curves for the remaining states are displayed in Figure 11 of Appendix E.

Table 1: MAE of methods in retrospective HFR estimation, and the associated percentage improvement on the convolutional ratio (CR) and lagged ratio (LR). Results are averaged over 51 regions and 10 replications.

	Lagged Ratio	Conv Ratio	Deconv-0	Deconv-1	Deconv-2	Deconv-T
MAE $\times 10^3$	16.9 ± 0.5	8.3 ± 0.1	6.5 ± 0.2	6.7 ± 0.2	6.9 ± 0.2	6.8 ± 0.2
Improv on CR (%)	-124.2 ± 5.3	0.0 ± 0.0	18.1 ± 1.1	17.1 ± 0.9	13.8 ± 1.0	15.7 ± 1.2
Improv on LR (%)	0.0 ± 0.0	46.3 ± 0.6	56.6 ± 0.8	56.1 ± 0.7	54.2 ± 0.8	55.1 ± 0.9

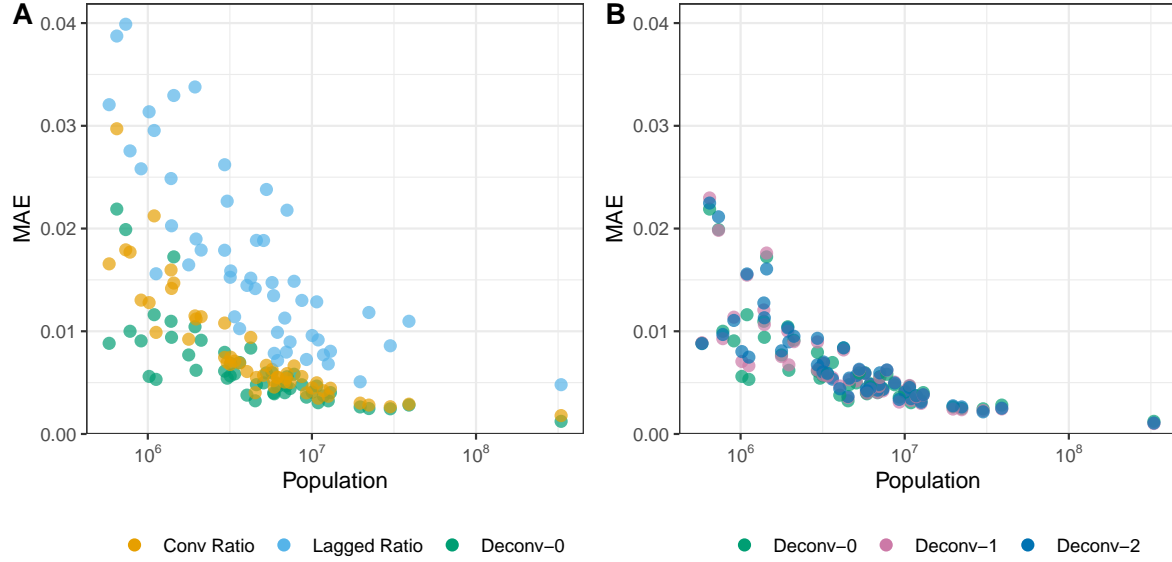


Figure 3: MAE versus population size in retrospective HFR estimation, for 51 regions (U.S. and 50 states). Each point is averaged over 10 replications.

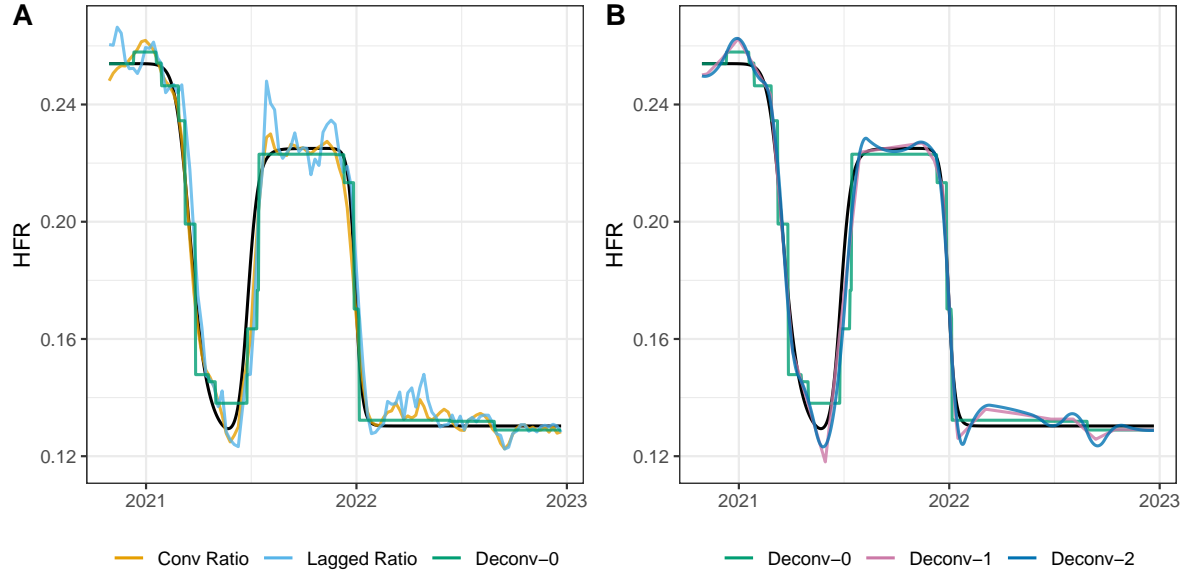


Figure 4: Example retrospective HFR estimates for Pennsylvania, from a single replication.

5.2 Real-time analysis

Deconvolution also performs strongly in the real-time setting. In the format of Table 1 above, Table 2 reports the MAEs and percentage improvements over the benchmarks in the real-time case, when all hyperparameters are tuned with cross-validation. Again, for each method we selected among the min and 1se rule depending on which resulted in more favorable performance; in the real-time case, this ends up being the 1se rule for all hyperparameters except for λ in deconvolution, which resulted in marginally better performance when tuned via the min rule. We note that the convolutional ratio estimator had substantially worse performance under the min rule, whose chosen window sizes tended to undersmooth counts.

As we can see from the table, the deconvolution methods provide an improvement in accuracy over the ratio-based methods, consistent with the previous results for the retrospective case. All orders m of trend filtering regularization are around 10-15% more accurate than the convolutional ratio, and around 30-35% better than the lagged ratio. Tuning the order of trend filtering still generally works well.

Figure 5 breaks down the MAE by population size, and once again we can see that deconvolution has an advantage over the ratio methods across the full range of geographies, with the gap being generally larger for smaller regions. Figure 6 displays example HFR curves for Pennsylvania, as before. In the current real-time case, we can clearly see the quality of all estimates degrade; the ratio-based estimates are especially volatile, and their erratic behavior here can be understood through the perspective of the analysis in [Goldwasser et al. \(2024\)](#). For example, their positive bias in early 2022, particularly the bias of the lagged ratio, can be attributed to Omicron surge which just passed. The deconvolution estimates are comparatively smoother and more stable. Finally, Figure 12 in Appendix E displays the full set of HFR curves across all states, where broadly the same conclusions are upheld.

5.3 Misspecification analysis

The advantage of deconvolution over benchmark methods persists under various degrees of misspecification. Figure 7 displays the MAE as a function of the offset of the mean of the working delay distribution used by each method (or the lag used by the lagged ratio) relative to the true delay. Unsurprisingly, we see accuracy degrade under misspecification, as evidenced by the curves which generally slope upwards as the mean offset moves away from zero. The gap in MAE of the lagged ratio and any of the other estimators is clearly large, regardless of the amount of misspecification. Comparing the convolutional ratio to deconvolution, the MAE gap narrows somewhat as the mean offset grows, in the retrospective case; on the other hand, the gap more or less holds steady as the mean offset varies, in the real-time case. Figure 13 in Appendix E transforms the MAE curves from deconvolution in Figure 7 into percentage improvement curves over the convolutional ratio. The findings are consistent and overall the deconvolution methods display comparably strong performance in our misspecified experiments.

6 Real data analysis

We now run the deconvolution and benchmark estimators on real COVID-19 hospitalization and death data from the state of Pennsylvania. To be clear, this differs from the analysis in the previous section which used real hospitalization counts, but simulated deaths generated from carefully-designed probabilistic models with synthetic underlying HFR curves. Hence, while in the current section we lack ground truth HFR curves for reference, we can still make qualitative comparisons between the estimates. Moreover, we can assess whether these patterns are consistent with our earlier findings, as well as with the general properties we expect the methods to exhibit.

For the real-time case, we used properly-versioned JHU deaths and NHSN hospitalizations. Retrospective estimation was more involved, as NCHS deaths were only reported weekly, but we seek to model HFR at the daily resolution. To address this, we imputed the daily deaths by sampling from a multinomial distribution with the weekly total as the number of trials and uniform probabilities (all equal to 1/7). JHU only reported deaths until March 2023, whereas NCHS continued reporting into early 2024. These dates determined the endpoints of our analysis.

We estimated the delay distributions in the same manner as in the simulated data (Section 4.1). Notice this strategy assumes that the delay distribution is stationary over time, which is likely not true. However,

Table 2: MAE of methods in real-time HFR estimation, and the associated percentage improvement on the convolutional ratio (CR) and lagged ratio (LR). Results are averaged over 51 regions and 10 replications.

	Lagged Ratio	Conv Ratio	Deconv-0	Deconv-1	Deconv-2	Deconv-T
MAE $\times 10^3$	33.9 ± 0.1	25.2 ± 0.1	20.7 ± 0.2	21.3 ± 0.2	22.0 ± 0.2	21.9 ± 0.2
Improv on CR (%)	-38.8 ± 0.7	0.0 ± 0.0	15.4 ± 0.5	12.3 ± 0.5	9.2 ± 0.5	10.2 ± 0.5
Improv on LR (%)	0.0 ± 0.0	24.5 ± 0.3	36.3 ± 0.5	34.0 ± 0.5	31.7 ± 0.5	32.5 ± 0.5

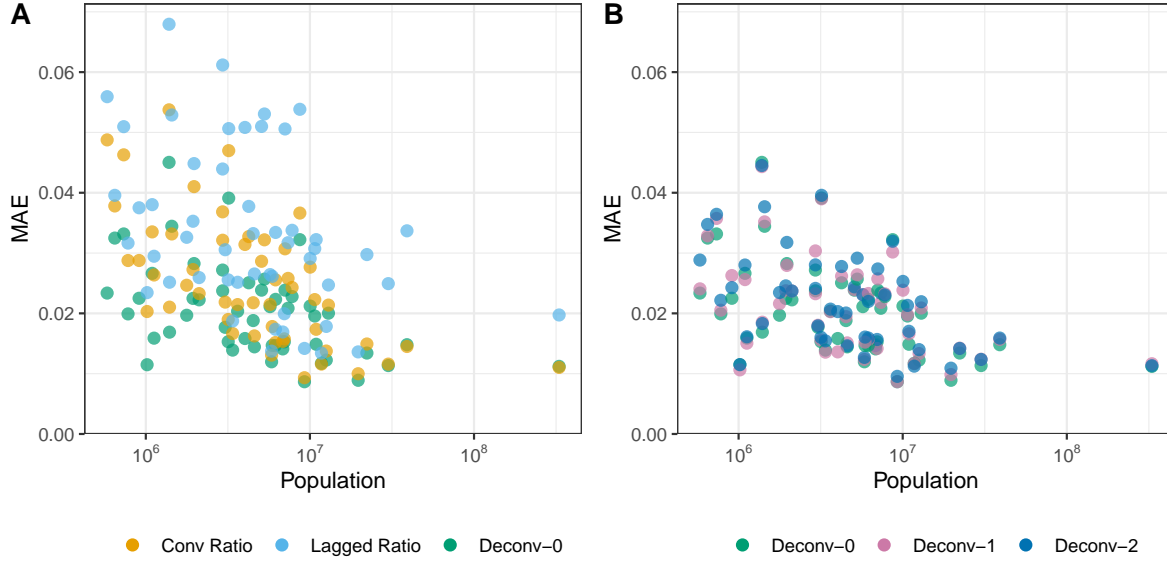


Figure 5: MAE versus population size in real-time HFR estimation, for 51 regions (U.S. and 50 states). Each point is averaged over 10 replications.

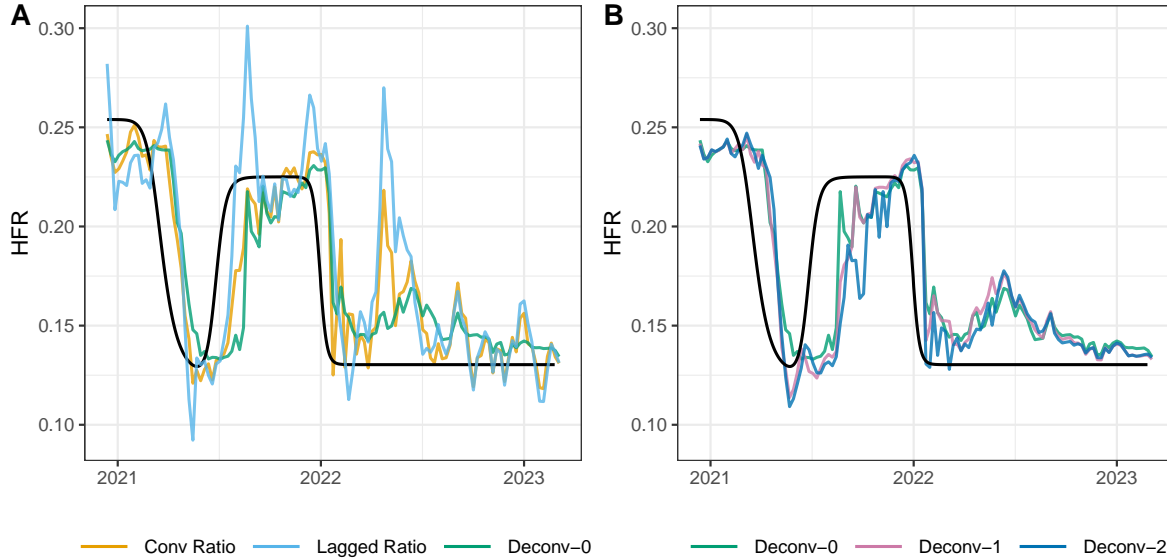


Figure 6: Example real-time HFR estimates for Pennsylvania, from a single replication.

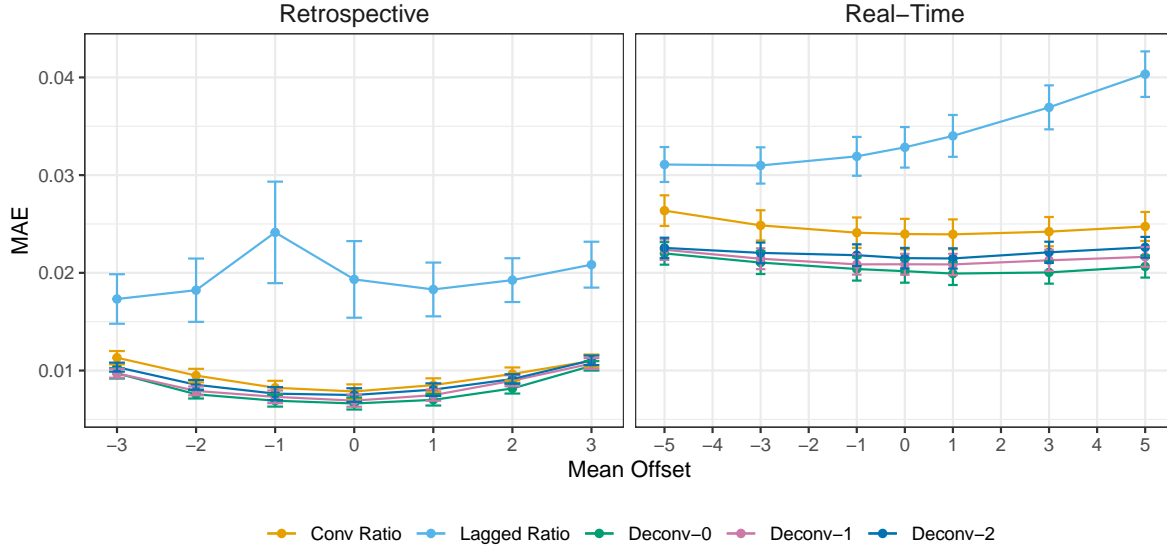


Figure 7: MAE versus mean offset, which is a measure of misspecification of the delay distribution. Results are averaged over 51 regions.

the purpose of these experiments is to draw comparisons on real data, not to estimate Pennsylvania’s severity rates as accurately as possible. Modeling the delay distribution more accurately, say, using (partial) line-list data, would likely improve results for all methods, but we do not pursue this direction.

Having no ground truth with which to measure MAE performance, we defaulted to tuning strategies that encourage more smoothness. Thus, we tuned all hyperparameters via the 1se rule (the only difference to the simulated data being that λ was tuned via the min rule for the deconvolution methods). As before, we used $K = 5$ folds for cross-validation and $M = 28$ folds for forward-validation.

Figure 8 displays the retrospective and real-time severity rate estimates. The high-level summary, across both settings (retrospective and real-time) and all methods, is as follows. We see HFRs peaking at around 30% during the surge around the beginning of 2021, then falling below 15% as the surge ended. Conditions remained relatively steady with the Alpha variant in spring 2021, then climbed rapidly with the Delta variant later that year. They dipped to around 20% as the Omicron variant swept through the state in winter 2022. As the wave passed, severity rates fell sharply, bottoming out around 10%. They remained around this level for the rest of the reporting period.

Comparing estimates to each another, the deconvolution estimates demonstrate notable stability relative to the ratio-based estimates. This is true in both retrospective and real-time cases, but especially pronounced in the real-time case. In the retrospective case, the lagged and convolutional ratios fluctuate between 7-12% throughout 2023, whereas deconvolution estimates remain steady, at any order m . The ratio-based estimates also *increase* as the Omicron wave ends in April 2022, whereas those from deconvolution smoothly decline. In the real-time case, the lagged and convolutional ratios display even more dramatic oscillations, and moreover, feature several large spikes. Their behavior here is consistent with the observations and analysis in [Goldwasser et al. \(2024\)](#). In contrast, the deconvolution estimates are much smoother, especially at order $m = 0$, and all orders avoid large spikes or (spurious) increases in HFR as the Omicron wave passes.

7 Discussion

In this work, we characterize the probabilistic relationship between two time series (primary and secondary event counts) which are related by time-varying convolution: a delay distribution times a quantity called the severity rate. The resulting likelihood allows us to construct new deconvolution-based estimators of severity rates, in both the retrospective and real-time settings. To encourage smoothness over time, we apply trend

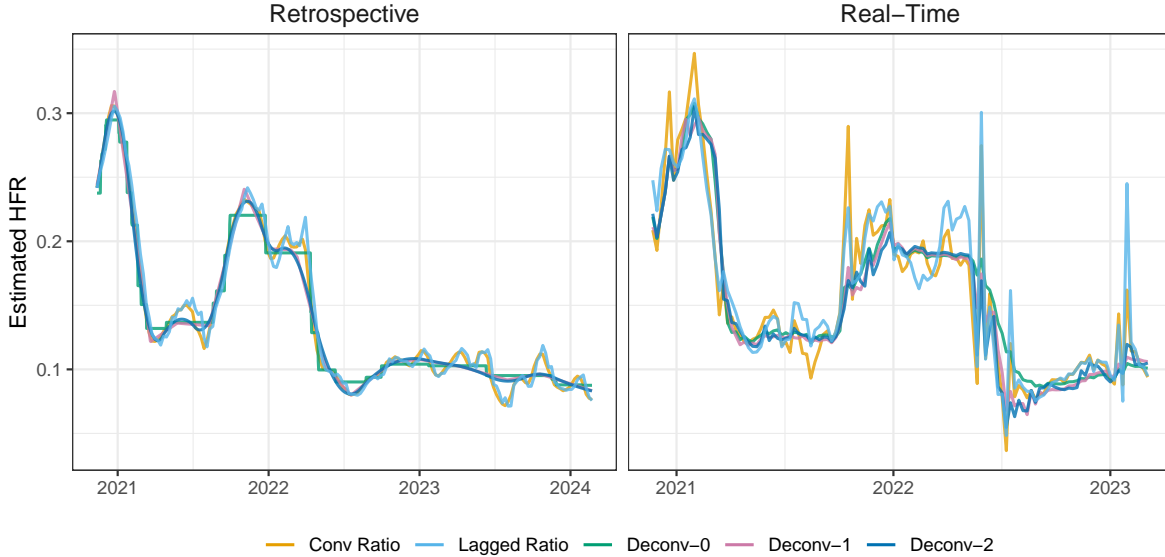


Figure 8: HFR estimates on real COVID-19 data in Pennsylvania.

filtering regularization, and in the real-time case, we use additional regularization to control volatility at the boundary of observations (the right tail of the time series). In extensive simulations, crafted to mimic the relationship between COVID-19 hospitalizations and deaths in the U.S., we find our deconvolution method to be consistently more accurate than the typical ratio-based methods used in practice, often by a significant margin. On real data, the qualitative differences are quite similar, with deconvolution able to provide stable estimates of the hospitalization fatality rate (HFR) under changing conditions, while the ratio-based estimates are subject to suspicious swings and spikes, as expected based on [Goldwasser et al. \(2024\)](#).

It is worth further reflecting on some of our results from the perspective of public health practice. In our experiments, cross-validation and the 1se rule—used to choose the smoothing window in the lagged ratio and convolutional ratio methods—nearly always selects the maximum window size of 4 weeks. Under smaller window sizes, the ratio-based methods perform much worse and the margin of improvement of deconvolution only grows. This creates a tradeoff to be navigated, as long windows may be undesirable in practice. A core purpose of real-time estimation is to expeditiously detect changes in severity rates. Smoothing values over an entire month seriously hampers our ability to do so, and it seems window sizes this large are rarely used in practice. The ability of trend filtering to perform locally adaptive smoothing—which effectively uses a longer or shorter smoothing window as needed at different parts of the time series—is a potentially powerful way to navigate the basic tradeoff between detecting changes and controlling variability.

We now reflect on some fundamental differences in the models underlying ratio-based and deconvolution-based methods. Notice that, as defined in (1), severity rates are inherently forward-looking quantities. The rate p_t is defined not only by primary events at t , but also by secondary events in the future. By maximizing an approximate likelihood, the deconvolution-based method thus automatically adopts this forward-looking perspective, even in the real-time case where future events are unobserved. In contrast, the real-time lagged and convolutional ratios from Section 4.2 are backward-looking methods. They quite literally looks backwards in time to past primary events in order to explain secondary events at t . To help draw this out precisely, we can define an analogous estimand, the backward-looking severity rate, by

$$\tilde{p}_t = \sum_{k=0}^d \mathbb{P}(\text{secondary event occurs at } t \mid \text{primary event at } t-k).$$

The original forward-looking severity rate admits a similar decomposition:

$$p_t = \sum_{k=0}^d \mathbb{P}(\text{secondary event occurs at } t+k \mid \text{primary event at } t).$$

In Appendix F, we develop connections between the real-time convolutional ratio and the backward-looking severity rate. A key point to highlight: if conditions remain constant—meaning, the delay distribution and severity rates are constant in a sufficiently large widow around t —then the forward- and backward-looking severity rates are equal, $\tilde{p}_t = p_t$, and the convolutional ratio is unbiased for this common value. Indeed, the real-time convolutional ratio performs well when the true severity rates are nearly constant. Looking back to Figure 6, its estimates tend to be most accurate during such periods, for example, in the last months of 2021, and throughout most of 2022.

However, when severity rates are nonstationary, the convolutional ratio suffers from bias. As shown in Goldwasser et al. (2024), this bias can be explained by studying the differences between the backward-looking rate \tilde{p}_t and forward-looking rate p_t . In part, the success of the deconvolution-based methods is due to the fact that they target the true forward-looking rate p_t , although it is challenging to precisely characterize the resulting improvement in bias for these methods. Of course, another significant component of their success is the regularization employed, which improves variance.

Interestingly, these forward- and backward-looking perspectives are mirrored in the literature on reproduction numbers, a central quantity in computational epidemiology. In broad terms, reproduction numbers convey the average number of secondary infections that will be produced from a single primary infection. Fraser (2007) uses the name “case reproduction number” for the forward perspective, measuring the effect of an infection at time t on future infections. In contrast, the “instantaneous reproduction number,” often denoted as R_t , is based on the backward perspective using secondary infections occurring at t due to primary infections that happened in the past. As with severity rates, the case and instantaneous reproduction numbers are equivalent under local stationarity. Most methods that estimate R_t in real-time target the instantaneous reproduction number (Bettencourt and Ribeiro, 2008; Cori et al., 2013; Parag, 2021). Recent work by Liu et al. (2024) proposes estimating instantaneous R_t in retrospect with trend filtering. This method could be adapted to the real-time setting using our additional regularization techniques. In addition, future work on R_t could estimate case reproduction numbers in real-time, using insights from our work on forward-looking severity rates. Case reproduction numbers may be more desirable as estimands than their instantaneous counterparts: they describe future dynamics of an epidemic in the most direct and intuitive way.

We close by mentioning a few more avenues for future work. A key component in practice is the delay distribution, whose misspecification can lead to degradation in performance. Without high-quality line list data, obtaining an accurate plug-in estimate is challenging. Jointly estimating this distribution along with the severity rates themselves would evade this challenge, posing an open methodological challenge. Li et al. (2023b) examine a joint estimation strategy for a different but broadly related deconvolution problem, based on the expectation-maximization (EM) algorithm. It would be interesting to study an analogous approach in our problem setting.

Another interesting direction would be to estimate severity rates disaggregated by different demographic groups, for example, severity rates for different age brackets. Conceivably, this could be done with the same primary or secondary event data (not requiring counts per demographic group) by employing a cohort-based model. This would feature a common set of severity rate curves (per demographic group) across all regions, and would then mix by known demographic proportions in each region to explain the effective severity rate in that region. A final direction of interest would be to produce confidence intervals for severity rates obtained using deconvolution and trend filtering penalties. In general, developing rigorous inferential tools on top of trend filtering remains a challenge, but promising recent developments in data fission/thinning (Leiner et al., 2025; Dharamshi et al., 2025) suggest there may be a path forward.

References

Ahmad, F. B. and Cisewski, J. A. (2025). Provisional COVID-19 mortality surveillance. National Center for Health Statistics.

Barbour, A. D. and Hall, P. (1984). On the rate of Poisson convergence. *Mathematical Proceedings of the Cambridge Philosophical Society*, 95(3):473–480.

Baud, D., Qi, X., Nielsen-Saines, K., Musso, D., Pomar, L., and Favre, G. (2020). Real estimates of mortality following COVID-19 infection. *Lancet Infectious Diseases*, 20(7):773.

Bellan, M., Patti, G., Hayden, E., Azzolina, D., Pirisi, M., et al. (2020). Fatality rate and predictors of mortality in an Italian cohort of hospitalized COVID-19 patients. *Scientific Reports*, 10:20731.

Bettencourt, L. M. A. and Ribeiro, R. M. (2008). Real time bayesian estimation of the epidemic potential of emerging infectious diseases. *PLOS One*, 3(5):e2185.

Cao, Y., Hiyoshi, A., and Montgomery, S. (2020). COVID-19 case-fatality rate and demographic and socioeconomic influencers: Worldwide spatial regression analysis based on country-level data. *BMJ Open*, 10(11):e043560.

Challen, R., Brooks-Pollock, E., Read, J. M., Dyson, L., Tsaneva-Atanasova, K., and Danon, L. (2021). Risk of mortality in patients infected with SARS-CoV-2 variant of concern 202012/1: Matched cohort study. *British Medical Journal*, 372:n579.

Charniga, K., Park, S. W., Akhmetzhanov, A. R., Cori, A., Dushoff, J., Funk, S., Gostic, K. M., Linton, N. M., Lison, A., Overton, C. E., Pulliam, J. R. C., Ward, T., Cauchemez, S., and Abbott, S. (2024). Best practices for estimating and reporting epidemiological delay distributions of infectious diseases using public health surveillance and healthcare data. arXiv:2405.08841.

Cori, A., Ferguson, N. M., Fraser, C., and Cauchemez, S. (2013). A new framework and software to estimate time-varying reproduction numbers during epidemics. *American Journal of Epidemiology*, 178(9):1505–1512.

COVID-19 Forecasting Team (2022). Variation in the COVID-19 infection–fatality ratio by age, time, and geography during the pre-vaccine era: A systematic analysis. *Lancet*, 399(10334):1469–1488.

Department of Health and Human Services (2023). COVID-19 guidance for hospital reporting and FAQs for hospitals, hospital laboratory, and acute care facility data reporting. <https://www.hhs.gov/sites/default/files/covid-19-faqs-hospitals-hospital-laboratory-acute-care-facility-data-reporting.pdf>.

Dharamshi, A., Neufeld, A., Motwani, K., Gao, L. L., Witten, D., and Bien, J. (2025). Generalized data thinning using sufficient statistics. *Journal of the American Statistical Association*, 120(549):511–523.

di Lego, V., Sánchez-Romero, M., and Prskawetz, A. (2022). The impact of COVID-19 vaccines on the case fatality rate: The importance of monitoring breakthrough infections. *International Journal of Infectious Diseases*, 119:178–183.

Dupé, F.-X., Fadili, J. M., and Starck, J.-L. (2011). Linear inverse problems with various noise models and mixed regularizations. In *Proceedings of the 5th International ICST Conference on Performance Evaluation Methodologies and Tools*.

Farrow, D. C., Brooks, L. C., Rumack, A., Tibshirani, R. J., and Rosenfield, R. (2015). Delphi Epidata API. <https://cmu-delphi.github.io/delphi-epidata/>.

Feng, J., Luo, H., Wu, Y., Zhou, Q., and Qi, R. (2023). A new method for accurate calculation of case fatality rates during a pandemic: Mathematical deduction based on population-level big data. *Infectious Medicine*, 2(2):96–104.

Fraser, C. (2007). Estimating individual and household reproduction numbers in an emerging epidemic. *PLOS One*, 2(8):1–12.

Garske, T., Legrand, J., Donnelly, C. A., Ward, H., Cauchemez, S., Fraser, C., Ferguson, N. M., and Ghani, A. C. (2009). Assessing the severity of the novel influenza A/H1N1 pandemic. *British Medical Journal*, 339:b2840.

Ghani, A. C., Donnelly, C. A., Cox, D. R., Griffin, J. T., Fraser, C., Lam, T. H., Ho, L. M., Chan, W. S., Anderson, R. M., Hedley, A. J., and Leung, G. M. (2005). Methods for estimating the case fatality ratio for a novel, emerging infectious disease. *American Journal of Epidemiology*, 162(5):479–486.

Goldwasser, J., Hu, A. J., Bilinski, A., McDonald, D. J., and Tibshirani, R. J. (2024). Challenges in estimating time-varying epidemic severity rates from aggregate data. *medRxiv*:24319518.

Goulart, P. J. and Chen, Y. (2024). Clarabel: An interior-point solver for conic programs with quadratic objectives. *arXiv*:2405.12762.

Hammond, J., Leister-Tebbe, H., Gardner, A., Abreu, P., Bao, W., Wisemandle, W., Baniecki, M., and Investigators, E.-H. (2022). Oral nirmatrelvir for high-risk, nonhospitalized adults with Covid-19. *The New England Journal of Medicine*, 386(15):1397–1408.

Hastie, T., Tibshirani, R., and Friedman, J. (2009). *The Elements of Statistical Learning: Data Mining, Inference and Prediction*. Springer, second edition.

Hodcroft, E. B. (2021). Covariants: SARS-CoV-2. <https://covariants.org/>.

Hong, Y. (2013). On computing the distribution function for the Poisson binomial distribution. *Computational Statistics & Data Analysis*, 59:41–51.

Horita, N. and Fukumoto, T. (2022). Global case fatality rate from COVID-19 has decreased by 96.8% during 2.5 years of the pandemic. *Journal of Medical Virology*, 95(1):e28231.

Jahja, M., Chin, A., and Tibshirani, R. J. (2022). Real-time estimation of COVID-19 infections: Deconvolution and sensor fusion. *Statistical Science*, 37(2):207–228.

Jewell, N. P., Lei, X., Ghani, A. C., Donnelly, C. A., Leung, G. M., Ho, L.-M., Cowling, B. J., and Hedley, A. J. (2007). Non-parametric estimation of the case fatality ratio with competing risks data: An application to Severe Acute Respiratory Syndrome (SARS). *Statistics in Medicine*, 26(9):1982–1998.

Kamp, J. and Krouse, S. (2020). Case-fatality metric points to increase in December deaths. *Wall Street Journal*.

Kim, J. and Lee, J.-H. (2017). The validation of a beta-binomial model for overdispersed binomial data. *Communications in Statistics: Simulation and Computation*, 46(2):807–814.

Kim, S.-J., Koh, K., Boyd, S., and Gorinevsky, D. (2009). ℓ_1 trend filtering. *SIAM Review*, 51(2):339–360.

Lasserre, J. B., Magron, V., Marx, S., and Zahm, O. (2021). Minimizing rational functions: A hierarchy of approximations via pushforward measures. *SIAM Journal on Optimization*, 31(3):2285–2306.

Leiner, J., Duan, B., Wasserman, L., and Ramdas, A. (2025). Data fission: Splitting a single data point. *Journal of the American Statistical Association*, 120(549):135–146.

Li, J.-X., Liao, P.-L., Wei, J. C.-C., Hsu, S.-B., and Yeh, C.-J. (2023a). A chronological review of COVID-19 case fatality rate and its secular trend and investigation of all-cause mortality and hospitalization during the Delta and Omicron waves in the United States: A retrospective cohort study. *Frontiers in Public Health*, 11:1143650.

Li, M., Li, J., Wang, K., and Li, L. M. (2023b). Reconstructing COVID-19 incidences from positive RT-PCR tests by deconvolution. *BMC Infectious Diseases*, 23:679.

Liu, J., Cai, Z., Gustafson, P., and McDonald, D. J. (2024). Time-varying reproduction number estimation with trend filtering. *PLOS Computational Biology*, 20(8):e1012324.

Liu, J., Wei, H., and He, D. (2023). Differences in case-fatality-rate of emerging SARS-CoV-2 variants. *Public Health in Practice*, 5:100350.

Lucy, L. B. (1974). An iterative technique for the rectification of observed distributions. *Astronomical Journal*, 79(6):745–754.

Luo, G., Zhang, X., Zheng, H., and He, D. (2021). Infection fatality ratio and case fatality ratio of COVID-19. *International Journal of Infectious Diseases*, 113:43–46.

Madrigal, A. C. and Moser, W. (2020). How many americans are about to die? *The Atlantic*.

McNeil, D. G. J. (2020). The pandemic's big mystery: How deadly is the coronavirus? *New York Times*.

Nishiura, H., Klinkenberg, D., Roberts, M., and Heesterbeek, J. A. P. (2009). Early epidemiological assessment of the virulence of emerging infectious diseases: A case study of an Influenza pandemic. *PLOS One*, 4(8):e6852.

Overton, C. E., Webb, L., Datta, U., Fursman, M., Hardstaff, J., Hiironen, I., Paranthaman, K., Riley, H., Sedgwick, J., Verne, J., Willner, S., Pellis, L., and Hall, I. (2022). Novel methods for estimating the instantaneous and overall COVID-19 case fatality risk among care home residents in England. *PLOS Computational Biology*, 18(10):e1010554.

Parag, K. V. (2021). Improved estimation of time-varying reproduction numbers at low case incidence and between epidemic waves. *PLOS Computational Biology*, 17(9):e1009347.

Qu, Y., Lee, C. Y., and Lam, K. F. (2022). A novel method to monitor COVID-19 fatality rate in real-time, a key metric to guide public health policy. *Scientific Reports*, 12:18277.

Rajgor, D. D., Lee, M. H., Archuleta, S., Bagdasarian, N., and Quek, S. C. (2020). The many estimates of the COVID-19 case fatality rate. *The Lancet Infectious Diseases*, 20(7):776–777.

Ramdas, A. and Tibshirani, R. J. (2016). Fast and flexible ADMM algorithms for trend filtering. *Journal of Computational and Graphical Statistics*, 25(3):839–858.

Reich, N. G., Lessler, J., Cummings, D. A. T., and Brookmeyer, R. (2012). Estimating absolute and relative case fatality ratios from infectious disease surveillance data. *Biometrics*, 68(2):598–606.

Reinhart, A., Brooks, L., Jahja, M., Rumack, A., Tang, J., Agrawal, S., Saeed, W. A., Arnold, T., Basu, A., Bien, J., Cabrera, A. A., Chin, A., Chua, E. J., Clark, B., Colquhoun, S., DeFries, N., Farrow, D. C., Forlizzi, J., Grabman, J., Gratzl, S., Green, A., Haff, G., Han, R., Harwood, K., Hu, A. J., Hyde, R., Hyun, S., Joshi, A., Kim, J., Kuznetsov, A., Motte-Kerr, W. L., Lee, Y. J., Lee, K., Lipton, Z. C., Liu, M. X., Mackey, L., Mazaitis, K., McDonald, D. J., McGuinness, P., Narasimhan, B., O'Brien, M. P., Oliveira, N. L., Patil, P., Perer, A., Politsch, C. A., Rajanala, S., Rucker, D., Scott, C., Shah, N. H., Shankar, V., Sharpnack, J., Shemetov, D., Simon, N., Smith, B. Y., Srivastava, V., Tan, S., Tibshirani, R., Tuzhilina, E., Nortwick, A. K. V., Ventura, V., Wasserman, L., Weaver, B., Weiss, J. C., Whitman, S., Williams, K., Rosenfeld, R., and Tibshirani, R. J. (2021). An open repository of real-time COVID-19 indicators. *Proceedings of the National Academy of Sciences*, 118(51):e2111452118.

Richardson, W. H. (1972). Bayesian-based iterative method of image restoration. *Journal of the Optical Society of America*, 62(1):55–59.

Rond, A., Giryes, R., and Elad, M. (2016). Poisson inverse problems by the plug-and-play scheme. *Journal of Visual Communication and Image Representation*, 41:96–108.

Roth, G. A., Emmons-Bell, S., Alger, H. M., Bradley, S. M., Das, S. R., de Lemos, J. A., Gakidou, E., Elkind, M. S. V., Hay, S., Hall, J. L., Johnson, C. O., Morrow, D. A., Rodriguez, F., Rutan, C., Shakil, S., Sorensen, R., Stevens, L., Wang, T. Y., Walchok, J., Williams, J., and Murray, C. (2021). Trends in patient characteristics and COVID-19 in-hospital mortality in the United States during the COVID-19 pandemic. *JAMA Network Open*, 4(5):e218828.

Rudin, L. I., Osher, S., and Fatemi, E. (1992). Nonlinear total variation based noise removal algorithms. *Physica D: Nonlinear Phenomena*, 60(1):259–268.

Tibshirani, R., Saunders, M., Rosset, S., Zhu, J., and Knight, K. (2005). Sparsity and smoothness via the fused lasso. *Journal of the Royal Statistical Society: Series B*, 67(1):91–108.

Tibshirani, R. J. (2014). Adaptive piecewise polynomial estimation via trend filtering. *Annals of Statistics*, 42(1):285–323.

Tibshirani, R. J. (2022). Divided differences, falling factorials, and discrete splines: Another look at trend filtering and related problems. *Foundations and Trends in Machine Learning*, 15(6):694–846.

Tibshirani, R. J. and Taylor, J. (2011). The solution path of the generalized lasso. *Annals of Statistics*, 39(3):1335–1371.

Ward, T. and Johnsen, A. (2021). Understanding an evolving pandemic: An analysis of the clinical time delay distributions of COVID-19 in the United Kingdom. *PLOS One*, 16(10):e0257978.

Wjst, M. and Wendtner, C. (2023). High variability of COVID-19 case fatality rate in Germany. *BMC Public Health*, 23:416.

Xia, Q., Yang, Y., Wang, F., Huang, Z., Qiu, W., and Mao, A. (2024). Case fatality rates of COVID-19 during epidemic periods of variants of concern: A meta-analysis by continents. *International Journal of Infectious Diseases*, 141:106950. Open access.

Xiao, A., Wu, F., Bushman, M., Zhang, J., Imakaev, M., Chai, P. R., Duvallet, C., Endo, N., Erickson, T. B., Armas, F., Arnold, B., Chen, H., Chandra, F., Ghaeli, N., Gu, X., Hanage, W. P., Lee, W. L., Matus, M., McElroy, K. A., Moniz, K., Rhode, S. F., Thompson, J., and Alm, E. J. (2022). Metrics to relate COVID-19 wastewater data to clinical testing dynamics. *Water Research*, 212:118070.

Xie, Y., Choi, T., and Al-Aly, Z. (2024). Mortality in patients hospitalized for COVID-19 vs Influenza in fall-winter 2023-2024. *Journal of the American Medical Association*, 331(22):1963–1965.

Yuan, J., Li, M., Lv, G., and Lud, Z. K. (2020). Monitoring transmissibility and mortality of COVID-19 in Europe. *Interational Joural of Infectious Diseases*, 95:311–315.

A Proof of Proposition 1

For the sake of clarity, this proof assumes the maximal secondary event time is d time steps after a primary event. However, this constraint is not necessary for the argument. By definition, $\mu_t = \sum_{k=0}^d X_{t-k} \pi_k^{(t-k)} p_{t-k}$ and $\mu_{t+1} = \sum_{k=0}^d X_{t+1-k} \pi_k^{(t+1-k)} p_{t+1-k}$. The first step is to bound the covariance:

$$\text{Cov}(Y_t, Y_{t+1} | X_{s \leq t+1}) = \mathbb{E}[Y_t Y_{t+1} | X_{s \leq t+1}] - \mu_t \mu_{t+1}.$$

Define the Bernoulli random variable $D_{s,t}^{(i)}$ as the indicator that the i^{th} individual with primary event at time s has secondary event at time t . With this notation,

$$Y_t = \sum_{k=0}^d \sum_{i=1}^{X_{t-k}} D_{t-k,t}^{(i)}, \quad \text{and} \quad Y_{t+1} = \sum_{\ell=0}^d \sum_{j=1}^{X_{t+1-\ell}} D_{t+1-\ell,t+1}^{(j)}.$$

Now partition the cross-terms of $\mathbb{E}[Y_t Y_{t+1} | X_{s \leq t+1}]$ into three pieces:

$$\begin{aligned} \mathbb{E}[Y_t Y_{t+1} | X_{s \leq t+1}] &= \mathbb{E} \left[\sum_{i=1}^{X_{t-d}} D_{t-d,t}^{(i)} \cdot \sum_{\ell=0}^d \sum_{j=1}^{X_{t+1-\ell}} D_{t+1-\ell,t+1}^{(j)} \right] + \mathbb{E} \left[\sum_{k=0}^d \sum_{i=1}^{X_{t-k}} D_{t-k,t}^{(i)} \cdot \sum_{j=1}^{X_{t+1}} D_{t+1,t+1}^{(j)} \right] \\ &\quad + \mathbb{E} \left[\sum_{k=0}^{d-1} \sum_{i=1}^{X_{t-k}} D_{t-k,t}^{(i)} \cdot \sum_{\ell=1}^d \sum_{j=1}^{X_{t+1-\ell}} D_{t+1-\ell,t+1}^{(j)} \right] \\ &= \left(X_{t-d} \pi_d^{(t-d)} p_{t-d} \right) \mu_{t+1} + \left(X_{t+1} \pi_0^{(t+1)} p_{t+1} \right) \mu_t \\ &\quad + \mathbb{E} \left[\sum_{k=0}^{d-1} \sum_{i=1}^{X_{t-k}} D_{t-k,t}^{(i)} \cdot \left(\sum_{\ell \neq k+1} \sum_{i=1}^{X_{t+1-\ell}} D_{t+1-\ell,t+1}^{(i)} + \sum_{j=1}^{X_{t-k}} D_{t-k,t+1}^{(j)} \right) \right]. \end{aligned}$$

The term on the final line may be further split into pieces, rewritten as:

$$\begin{aligned} &\sum_{k=0}^{d-1} X_{t-k} \pi_k^{(t-k)} p_{t-k} \sum_{\ell \neq k+1} X_{t+1-\ell} \pi_{\ell}^{(t+1)} p_{t+1-\ell} + \mathbb{E} \left[\sum_{k=0}^{d-1} \sum_{i=1}^{X_{t-k}} D_{t-k,t}^{(i)} \cdot \sum_{j=1}^{X_{t-k}} D_{t-k,t+1}^{(j)} \right] \\ &= \sum_{k=0}^{d-1} X_{t-k} \pi_k^{(t-k)} p_{t-k} \sum_{\ell \neq k+1} X_{t+1-\ell} \pi_{\ell}^{(t+1)} p_{t+1-\ell} \\ &\quad + \sum_{k=0}^{d-1} \sum_{i=1}^{X_{t-k}} \mathbb{E} \left[D_{t-k,t}^{(i)} \sum_{j \neq i} D_{t-k,t+1}^{(j)} \right] + \sum_{k=0}^{d-1} \sum_{i=1}^{X_{t-k}} \mathbb{E} \left[\underbrace{D_{t-k,t}^{(i)} D_{t-k,t+1}^{(i)}}_{\text{mutually exclusive}} \right] \\ &= \sum_{k=0}^{d-1} X_{t-k} \pi_k^{(t-k)} p_{t-k} \left(\sum_{\ell \neq k+1} X_{t+1-\ell} \pi_{\ell}^{(t+1-\ell)} p_{t+1-\ell} + (X_{t-k} - 1) \pi_{k+1}^{(t-k)} p_{t-k} \right) \\ &= \sum_{k=0}^{d-1} \sum_{\ell=0}^{d-1} \left(X_{t-k} \pi_k^{(t-k)} p_{t-k} \right) \left(X_{t-\ell} \pi_{\ell+1}^{(t-\ell)} p_{t-\ell} \right) - \sum_{k=0}^{d-1} X_{t-k} \left(\pi_k^{(t-k)} \pi_{k+1}^{(t-k)} \right) p_{t-k}^2. \end{aligned}$$

So putting all parts together,

$$\begin{aligned} \mathbb{E}[Y_t Y_{t+1} | X_{s \leq t+1}] &= \left(X_{t-d} \pi_d^{(t-d)} p_{t-d} \right) \mu_{t+1} + \left(X_{t+1} \pi_0^{(t+1)} p_{t+1} \right) \\ &\quad + \sum_{k=0}^{d-1} \sum_{\ell=0}^{d-1} \left(X_{t-k} \pi_k^{(t-k)} p_{t-k} \right) \left(X_{t-\ell} \pi_{\ell+1}^{(t-\ell)} p_{t-\ell} \right) - \sum_{k=0}^{d-1} X_{t-k} \left(\pi_k^{(t-k)} \pi_{k+1}^{(t-k)} \right) p_{t-k}^2 \\ &= \underbrace{\left(\sum_{k=0}^d X_{t-k} \pi_k^{(t-k)} p_{t-k} \right)}_{\mu_t} \underbrace{\left(\sum_{\ell=0}^d X_{t+1-\ell} \pi_{\ell}^{(t+1-\ell)} p_{t+1-\ell} \right)}_{\mu_{t+1}} - \sum_{k=0}^{d-1} X_{t-k} \left(\pi_k^{(t-k)} \pi_{k+1}^{(t-k)} \right) p_{t-k}^2, \end{aligned}$$

and therefore,

$$\text{Cov}(Y_t, Y_{t+1} | X_{s \leq t+1}) = \mathbb{E}[Y_t Y_{t+1} | X_{s \leq t+1}] - \mu_t \mu_{t+1} = - \sum_{k=0}^{d-1} X_{t-k} \left(\pi_k^{(t-k)} \pi_{k+1}^{(t-k)} \right) p_{t-k}^2.$$

We can see that the correlation clearly must be nonpositive. To lower bound the correlation, assume equal (conditional) variances at times t and $t+1$. Then

$$\begin{aligned} \text{Cor}(Y_t, Y_{t+1} | X_{s \leq t}) &= \frac{\text{Cov}(Y_t, Y_{t+1} | X_{s \leq t})}{\text{Var}(Y_t | X_{s \leq t})} \\ &= - \frac{\sum_{k=0}^{d-1} X_{t-k} \pi_k^{(t-k)} \pi_{k+1}^{(t-k)} p_{t-k}^2}{\sum_{k=0}^d X_{t-k} \pi_k^{(t-k)} p_{t-k} (1 - \pi_k^{(t-k)} p_{t-k})} \\ &\geq - \frac{(\max_{k \geq 0} \pi_k^{(t-k)} p_{t-k}) \sum_{k=0}^{d-1} X_{t-k} \pi_k^{(t-k)} p_{t-k}}{(1 - \max_{k \geq 0} \pi_k^{(t-k)} p_{t-k}) \sum_{k=0}^{d-1} X_{t-k} \pi_k^{(t-k)} p_{t-k}} \\ &= - \frac{\max_{k \geq 0} \pi_k^{(t-k)} p_{t-k}}{1 - \max_{k \geq 0} \pi_k^{(t-k)} p_{t-k}}. \end{aligned}$$

B Gaussian deconvolution filtering

The Gaussian approximation is an alternative to the Poisson approximation to the Poisson-binomial. It uses a mean μ_t and variance σ_t^2 as defined in (5). With the corresponding Gaussian log likelihood in place of the Poisson log likelihood, the retrospective optimization problem (7) becomes

$$\underset{0 \leq p \leq 1}{\text{minimize}} \sum_t \left[\left(\log \widehat{\sigma}_t^2(p) + \frac{1}{\widehat{\sigma}_t^2(p)} \left(Y_t - \sum_{k=0}^d X_{t-k} \widehat{\pi}_k^{(t-k)} p_{t-k} \right)^2 \right) + \lambda \|D^{(m+1)} p\|_1 \right],$$

where $\widehat{\sigma}_t^2(p) = \sum_{k=0}^{\infty} X_{t-k} \widehat{\pi}_k^{(t-k)} p_{t-k} (1 - \pi_k^{(t-k)} p_{t-k})$. The above is a nonconvex problem, hence to simplify computation, we drop the log term and approximate $\widehat{\sigma}_t^2(p)$ by an estimate $\widehat{\mu}_t$ of the mean, motivated by the fact that in our problem setting, σ_t^2 is close to μ_t (recall the discussion in Section 2.1). The estimate $\widehat{\mu}_t$ can be obtained by nonparametric smoothing of the secondary event time series Y_t , and can therefore be treated as fixed (not depending on p) in the optimization. This results in

$$\underset{0 \leq p \leq 1}{\text{minimize}} \sum_t \frac{1}{\widehat{\mu}_t} \left(Y_t - \sum_{k=0}^d X_{t-k} \widehat{\pi}_k^{(t-k)} p_{t-k} \right)^2 + \lambda \|D^{(m+1)} p\|_1,$$

for the Gaussian retrospective deconvolution estimator. The real-time estimator is defined similarly, simply appending the additional regularization terms as in (8).

In experiments not shown, we found that the Gaussian model for deconvolution performed similarly but marginally worse than the Poisson model. With constant order ($m = 0$), the average performance was nearly as strong as that of the Poisson model. However, it was somewhat worse on higher orders, especially in the real-time case. We did not find significant gaps in performance when analyzing by region population. Finally, Gaussian deconvolution was not hindered by its use of the plug-in estimate $\widehat{\mu}_t$ of the variance. We also ran experiments with the true (fixed) variance was used in lieu of $\widehat{\mu}_t$, and the performance was very similar.

C Derivation of λ_{\max}

Consider first the general optimization problem, for a differentiable convex loss ℓ , matrix D , and norm $\|\cdot\|$,

$$\underset{\theta}{\text{minimize}} \ell(\theta) + \lambda \|D\theta\|. \quad (10)$$

The first-order optimality conditions determining a solution $\widehat{\theta}$ are

$$-\nabla \ell(\widehat{\theta}) = \lambda D^T v, \quad \text{where } v \in \partial \|D\widehat{\theta}\|, \quad (11)$$

where $\nabla\ell(\theta)$ denotes the gradient of ℓ at θ , and $\partial\|D\hat{\theta}\|$ denotes the subdifferential (the set of subgradients) of $\|\cdot\|$ at $D\hat{\theta}$. Suppose that

$$\lambda \geq \underbrace{\min \left\{ \|(D^\top)^+ \nabla\ell(\theta) + \eta\|_* : \theta \in \text{null}(D), \eta \in \text{row}(D) \right\}}_{\lambda_{\max}}, \quad (12)$$

where $\text{null}(D)$ denotes the null space of D , $\text{row}(D)$ denotes the row space of D , $(D^\top)^+$ denotes the generalized inverse of D^\top , and $\|\cdot\|_*$ denotes the dual norm to $\|\cdot\|$. If $\hat{\theta}, \hat{\eta}$ denotes a solution to the above minimization determining λ_{\max} , then

$$v = \frac{-(D^\top)^+ \nabla\ell(\hat{\theta}) + \hat{\eta}}{\lambda}$$

is a valid subgradient of $\|\cdot\|$ at $D\hat{\theta} = 0$, because $\|v\|_* = \|(D^\top)^+ \nabla\ell(\hat{\theta}) + \hat{\eta}\|_*/\lambda \leq 1$ (note the subdifferential of $\|\cdot\|$ at 0 is precisely the unit ball in the dual norm, centered at the origin). In other words, the pair $\hat{\theta}, v$ solves the first-order conditions (11) and $\hat{\theta}$ solves (10).

We now inspect λ_{\max} as defined in (12) for the Poisson linear inverse problem (7). Write A for the linear operator such that

$$(Ap)_t = \sum_{k=0}^d X_{t-k} \hat{\pi}_k^{(t-k)} p_{t-k},$$

and Y for the vector of secondary event counts. Then the Poisson linear inverse loss can be expressed as

$$\ell(p) = 1^\top Ap - Y^\top \log(Ap),$$

where 1 denotes the vector of all 1s, and $\log(Ap)$ is interpreted as elementwise application of \log . Hence

$$\nabla\ell(p) = A^\top(1 - Y/Ap),$$

where Y/Ap is interpreted as elementwise division. Abbreviating $D = D^{(m+1)}$, this matrix always will always be full row rank, and thus $(D^\top)^+ = (DD^\top)^{-1}D^\top$. Then, with $\|\cdot\| = \|\cdot\|_1$ and $\|\cdot\|_* = \|\cdot\|_\infty$, note that

$$\lambda_{\max} = \min \left\{ \|(DD^\top)^{-1}D^\top A^\top(1 - Y/Ap) + \eta\|_\infty : p \in \text{null}(D), \eta \in \text{row}(D), 0 \preceq p \preceq 1 \right\}.$$

Setting $\eta = 0$ and $p = B\alpha$, where B is a matrix whose columns span $\text{null}(D)$ —which for the trend filtering penalty matrix is the space of polynomials of degree m —we obtain a simpler upper bound

$$\lambda_{\max} \leq \min \left\{ \|(DD^\top)^{-1}D^\top A^\top(1 - Y/AB\alpha)\|_\infty : 0 \preceq B\alpha \preceq 1 \right\}. \quad (13)$$

This reduces to rational optimization (sum of ratio of polynomials), since we can equivalently write it as

$$\lambda_{\max} \leq \min \left\{ \max_s \left| \sum_t [(DD^\top)^{-1}D^\top A^\top]_{st} \left(1 - \frac{Y_t}{\sum_{k=0}^d X_{t-k} \hat{\pi}_k^{(t-k)} g(t-k)} \right) \right| : g \text{ is a degree } m \text{ polynomial with } 0 \leq g \leq 1 \right\}.$$

In principle, this upper bound should be computable to arbitrary accuracy using SDP relaxation techniques (Lasserre et al., 2021), though this is likely to be difficult in practice. Instead, we can rewrite (13) once more as a min-max problem,

$$\lambda_{\max} \leq \min_{0 \preceq B\alpha \preceq 1} \max_{\|u\|_1 \leq 1} u^\top (DD^\top)^{-1} D^\top A^\top (1 - Y/AB\alpha),$$

and then use alternating optimization to approximate the solution. That is, we iteratively take a (projected) gradient step with respect to α , and perform exact minimization over u (which is easy, since $u^\top x$ for a fixed vector x is minimized over all $\|u\|_1 \leq 1$ by taking $u = \text{sign}(x_i)e_i$, where $|x_i| = \|x\|_\infty$ and e_i is the i^{th} canonical basis vector). Note that after any number of iterations of alternating minimization, we can take the resulting α and plug this into (13) to obtain a valid upper bound.

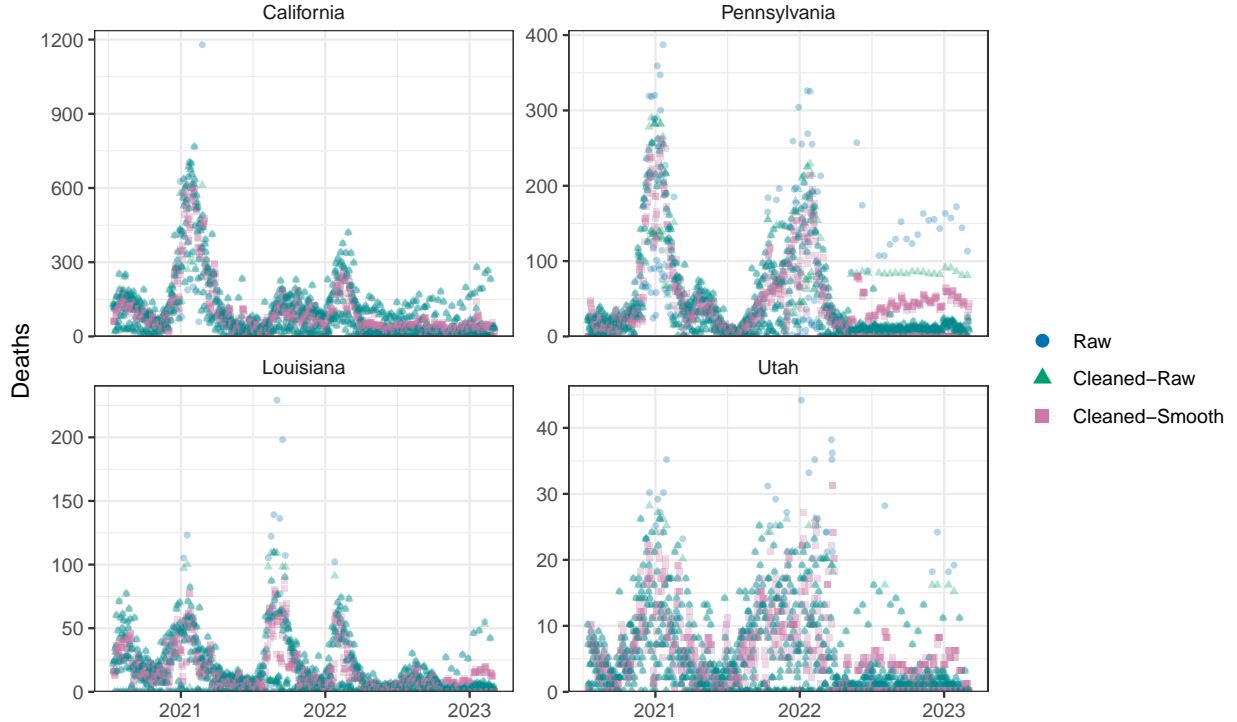


Figure 9: Raw JHU deaths and the results of two cleaning approaches. The green triangles are the result of detecting and correcting outliers directly based on the raw data; the pink squares are the result of a process which first smooths the data before dealing with outliers, and then “unsmooths”, as described in the text.

D Further experimental details

D.1 Cleaning JHU deaths

Before estimating the dispersion for our beta-binomial simulation model, it was necessary to preprocess the JHU death data. The raw data contained many outliers, as shown in the blue circles in Figure 9. Often, large numbers of previously unreported counts were dumped on a certain day. Low outliers were also prevalent, for example holidays or negative values to revert cumulative numbers after accounting for duplicate reports. To deal with these issues, we preprocessed the data to remove outliers. First, we identified obvious data dumps: stretches of 6 days with 0 counts followed by a nonzero value. We distributed this value backward over the trailing 7 days, allocating uniformly with a multinomial sampler. Similarly, we redistributed negative counts over the entire preceding history, again with a uniform multinomial sampler.

Many outliers remained after this basic preprocessing. To further reduce noise, we applied the following outlier truncation procedure. At each time point, we computed the median value over a centered window and defined a tolerance band around this local median curve based on the interquartile range of residuals. Values lying outside this band were pulled back to the nearest boundary, preserving local structure while shrinking extreme deviations. This procedure produced the green triangles in Figure 9, which as we can see, effectively removed large outliers, such as the two highest counts in Louisiana. However, this generally failed to address the systematic biases in the data.

Specifically, it did not address day-of-week effects, in which death counts were systematically under- or over-reported on certain days of the week. For example, many states reported fewer deaths on the weekends, instead tallying them early in the following week. Day-of-week effects are present in all four states shown in Figure 9, where in some instances, counts oscillate between 0 and large positive values, even in the cleaned version of the data described in the above paragraph. The outlier detection rule did not flag the lower values

here as outlying because they occurred frequently enough to be encompassed in the IQR.

We therefore settled on an alternative strategy, consisting of the following steps. First, we first smoothed the data using a 7-day trailing average, which effectively removed day-of-week effects (since each day of the week is incorporated into each average). We then ran the outlier truncation procedure, which still corrected a number of values. Finally, we estimated the mean curve using a smoothing spline, computed the residuals to the 7-day averaged data, and added a rescaled version of these residuals—where we multiply by $\sqrt{7}$ —back to the mean curve in order to produce cleaned data with appropriate daily-level variability. This produced the pink squares in Figure 9. The resulting counts are concentrated at intermediate values during “split” periods, where the original counts oscillate between low and high values, and display a reasonable degree of variability. We believe this is an effective approach to clean data for our purposes here (with the eventual goal being to estimate dispersion), but do not suggest it be seen as a general-purpose data cleaning technique.

D.2 Beta-binomial distribution

Like the Poisson-binomial distribution, the beta-binomial is supported on integers between 0 and the number of trials. This distribution counts the number of successes among independent Bernoulli trials whose success probabilities are drawn from a given beta distribution, whose parameters reflect the amount of overdispersion. For n trials, the beta-binomial distribution is often written as $\text{BetaBinom}(n, M, \rho)$, which is called mean-rho parameterization. Here $M \in (0, 1)$ is the average probability of success, and $\rho \in [0, 1]$ controls the degree of overdispersion. (Another formulation is $\text{BetaBinom}(n, \alpha, \beta)$, where α, β parameterize the beta distribution; there is a one-to-one relation between the two parameterizations: $M = \alpha/(\alpha + \beta)$, and $\rho = 1/(\alpha + \beta + 1)$.) The distribution $\text{BetaBinom}(n, M, \rho)$ has mean $\mu = nM$ and variance

$$\sigma^2 = nM(1 - M)[1 + (n - 1)\rho].$$

Rearranging the variance expression reveals

$$\rho = \left(\frac{\sigma^2}{nM(1 - M)} - 1 \right) \left(\frac{1}{n - 1} \right). \quad (14)$$

In our severity rate estimation context, the number of secondary events at each time t is approximated by a beta-binomial variate. Recall that its mean μ_t is as in (5). The number of trials n_t at t is the total primary incidence over the previous d days, that is, the pool of individuals who may have a secondary event at t . The average success probability at t is thus

$$M_t = \frac{\mu_t}{n_t} = \frac{\mu_t}{\sum_{k=0}^d X_{t-k}},$$

which explains the first expression in (9). Furthermore, given the Poisson-binomial variance σ_t^2 in (5), and a dispersion factor $\hat{\beta}$, the variance of secondary incidence is thus $\hat{\beta}\sigma_t^2$. Plugging this variance into (14) confirms the second expression in (9).

D.3 Misspecified delay distributions

Figure 10 displays the misspecified delay distributions used in our experiments. The black line is the original delay distribution, whereas the colored ones have varying degrees of misspecification. The delay distributions differ across states, since their means depend on the correlation between primary and secondary events. We choose to visualize California, Louisiana, and Wyoming as a representative trio because they are the largest, roughly median, and smallest state by population, respectively.

E Further experimental results

Table 3 displays the MAE results for retrospective estimation, now under oracle tuning, where we select the best hyperparameters for each method to minimize the average MAE (over all regions and replications). The results are even more favorable to the deconvolution methods, compared to those from cross-validation tuning in Table 1.

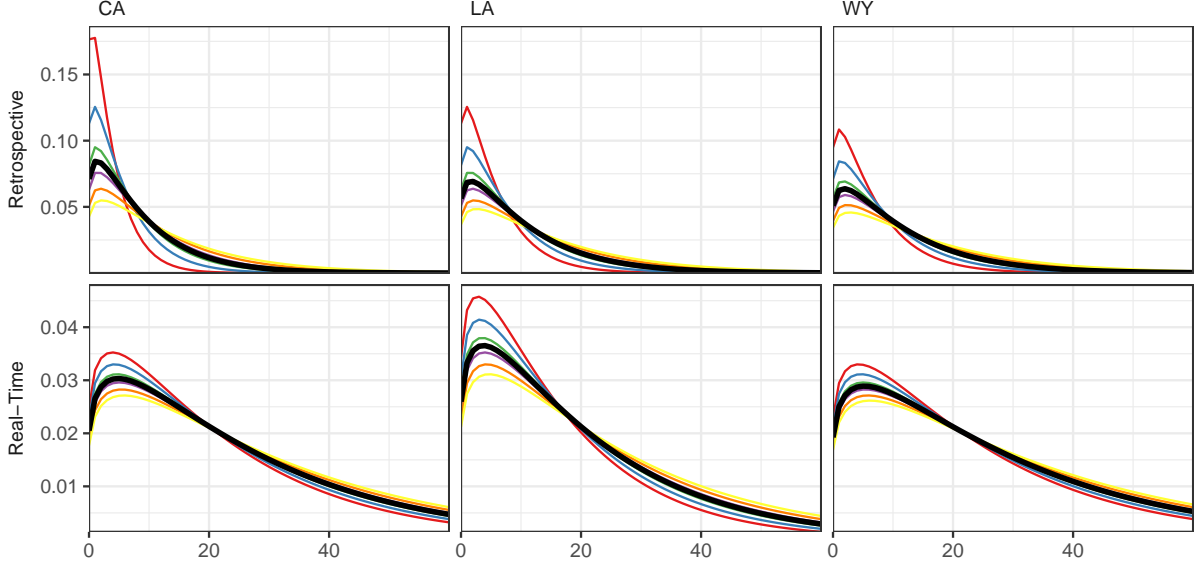


Figure 10: Example misspecified delay distributions, for three states, as we vary the mean (which recall is tied to the variance), in both retrospective and real-time simulation models.

Table 3: MAE of methods in retrospective HFR estimation, and the associated percentage improvement on the convolutional ratio (CR) and lagged ratio (LR), under oracle tuning. Compare to Table 1.

	Lagged Ratio	Conv Ratio	Deconv-0	Deconv-1	Deconv-2	Deconv-T
MAE $\times 10^3$	12.5 ± 0.1	8.2 ± 0.1	5.7 ± 0.1	5.8 ± 0.1	5.9 ± 0.1	5.7 ± 0.1
Improv on CR (%)	-67.3 ± 0.8	0.0 ± 0.0	23.7 ± 0.5	25.5 ± 0.4	23.7 ± 0.4	24.7 ± 0.5
Improv on LR (%)	0.0 ± 0.0	35.5 ± 0.3	51.7 ± 0.4	52.5 ± 0.4	51.4 ± 0.4	52.2 ± 0.4

Figures 11 and 12 show the retrospective and real-time HFR estimates, respectively, for all 50 states. As in Figures 4 and 6 in the main text, deconvolution and the convolutional ratio use the oracle delay distribution, the lagged ratio uses the oracle lag, and the hyperparameters all are tuned via cross-validation. All orders of trend filtering regularization are displayed. Overall, we see that the deconvolution estimators are more stable than the ratio estimators; they capture changes in HFR quickly, and for the most part, do not exhibit the same spurious oscillations.

Figure 13 displays the performance relative to the convolutional ratio for misspecified delay distributions. This is analogous to Figure 7 in the main text. The results show that the deconvolution approach maintains an advantage over the convolutional ratio for varying degrees of misspecification, with the exception of large positive mean offsets in the retrospective case, where this advantage is somewhat erased.

F Backward-looking severity rates

We provide two connections between the real-time convolutional ratio and the backward-looking severity rate. Recall the backward-looking severity rate is defined as

$$\tilde{p}_t = \sum_{k=0}^d \mathbb{P}(\text{secondary event occurs at } t \mid \text{primary event at } t-k) = \sum_{k=0}^d \pi_k^{(t-k)} p_{t-k},$$

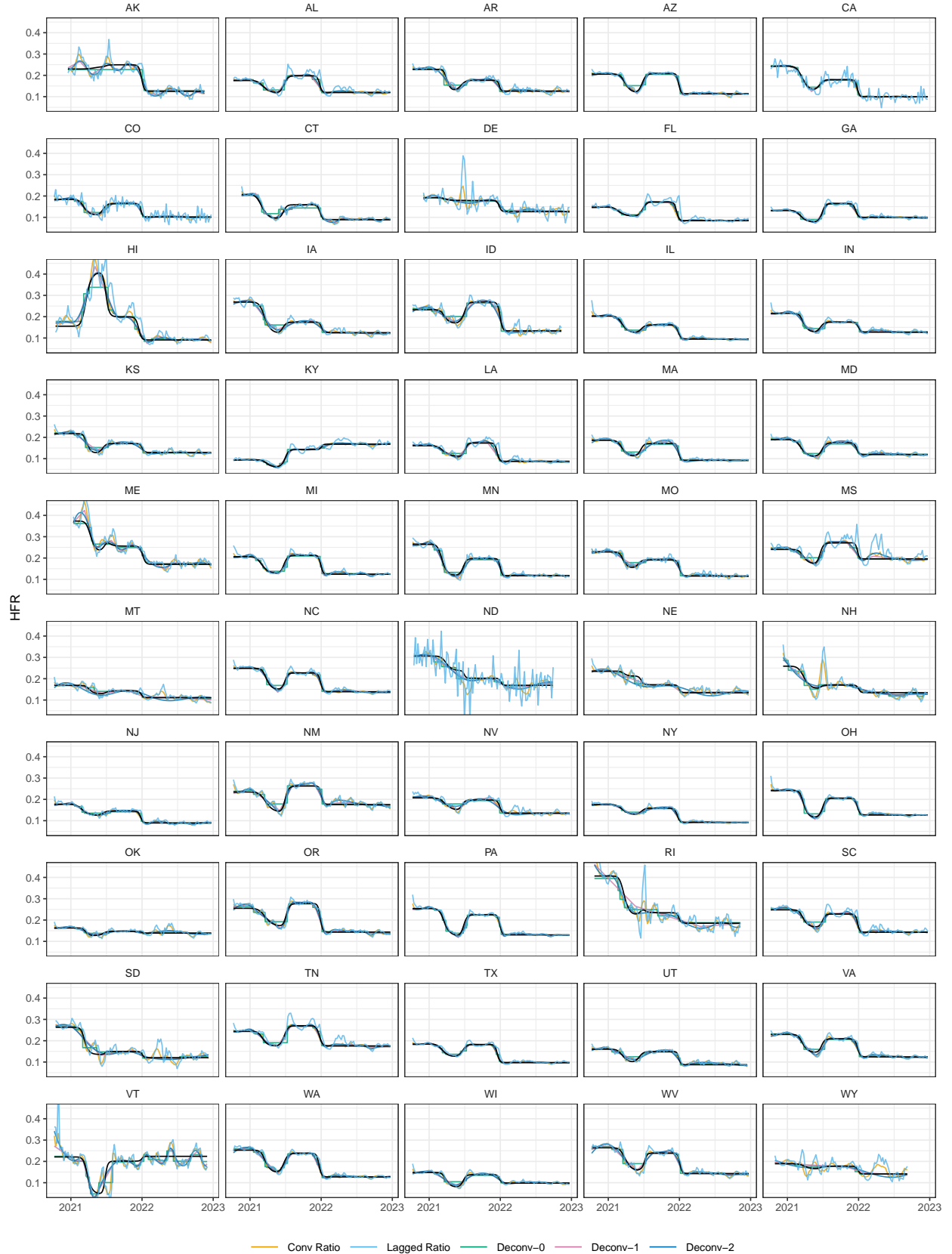


Figure 11: Retrospective HFR estimates for all 50 states.

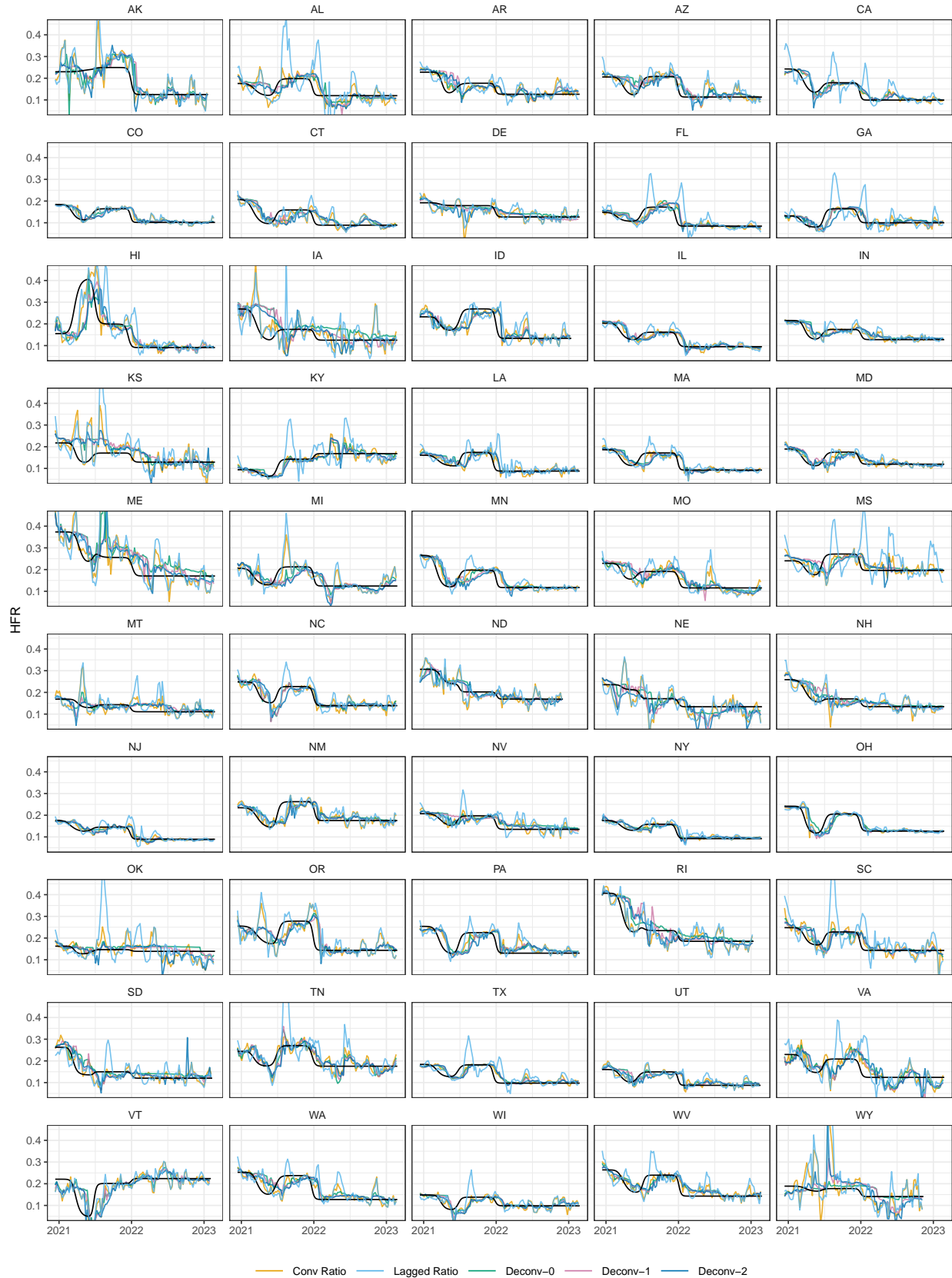


Figure 12: Real-time HFR estimates for all 50 states.

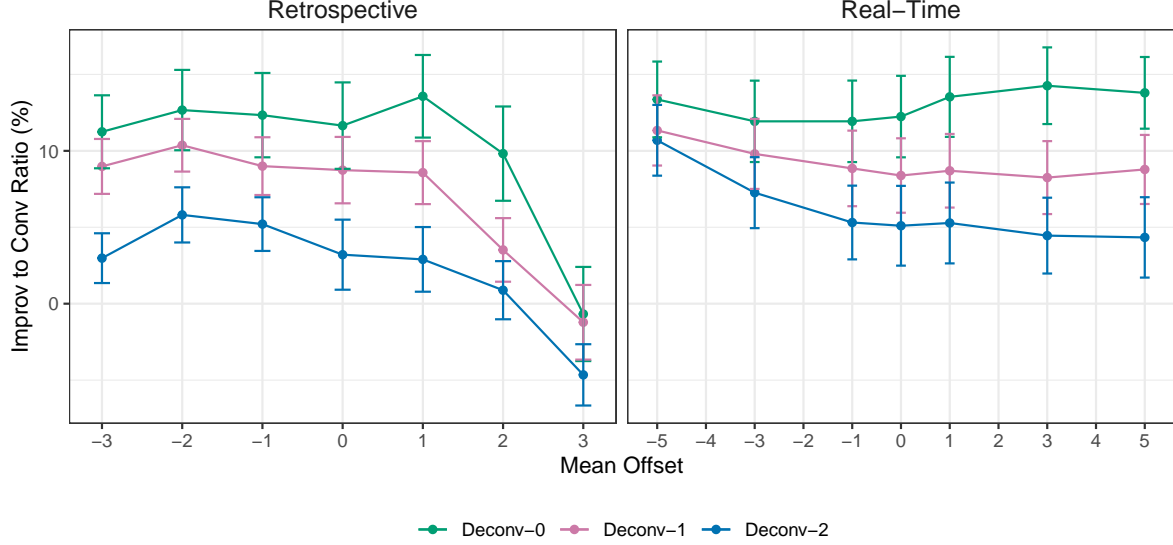


Figure 13: Percentage improvement of deconvolution to the convolutional ratio as a function of mean offset in the misspecified case. Compare to Figure 7.

and the original forward-looking severity rate is

$$p_t = \sum_{k=0}^d \mathbb{P}(\text{secondary event occurs at } t+k \mid \text{primary event at } t) = \sum_{k=0}^d \pi_k^{(t)} p_t.$$

For the sake of simplicity, assume throughout that the delay distributions before t , occurring in any of the summands above, are equal to a constant distribution π . In the real-time case, using the oracle delay π , the convolutional ratio (using raw, not smoothed counts) has conditional expectation:

$$\mathbb{E}[\hat{p}_t \mid X_{s \leq t}] = \frac{\sum_{k=0}^d X_{t-k} \pi_k p_{t-k}}{\sum_{k=0}^d X_{t-k} \pi_k} = \sum_{k=0}^d \frac{X_{t-k}}{\sum_{j=0}^d X_{t-j} \pi_j} \pi_k p_{t-k}.$$

First, assume that primary counts are equal to a constant X_0 in the d time points preceding t . Note that the convolutional ratio reduces to Y_t/X_0 , which is unbiased for the backwards rate:

$$\mathbb{E}[\hat{p}_t \mid X_{s \leq t}] = \sum_{k=0}^d \frac{X_0}{\sum_{j=0}^d X_0 \pi_j} \pi_k p_{t-k} = \sum_{j=0}^d \pi_k p_{t-k} = \tilde{p}_t.$$

Instead, assume that severity rates are equal to a constant p_0 in the d time points preceding t . As the delay distributions are constant, this implies

$$\begin{aligned} \mathbb{P}(\text{secondary event occurs at } t \mid \text{primary event at } t-k) \\ = \mathbb{P}(\text{secondary event occurs at } t+k \mid \text{primary event at } t), \end{aligned}$$

for each $k = 0, \dots, d$. This means that the backward- and forward-looking rates are equivalent, $\tilde{p}_t = p_t = p_0$. Furthermore, the convolutional ratio is unbiased for this common value:

$$\mathbb{E}[\hat{p}_t \mid X_{s \leq t}] = \frac{\sum_{k=0}^d X_{t-k} \pi_k p_{t-k}}{\sum_{k=0}^d X_{t-k} \pi_k} = p_0 \frac{\sum_{k=0}^d X_{t-k} \pi_k}{\sum_{k=0}^d X_{t-k} \pi_k} = p_0.$$